Cellular Uptake and Magneto-Hyperthermia Induced Cytotoxicity using Photoluminescent Fe_3O_4 Nanoparticle/Si Quantum Dot Hybrids

Morteza Javadi,[1#] Van A. Ortega,[2#] Alyxandra N. Thiessen,[1#] Maryam Aghajamali,[1] Muhammad Amirul Islam,[1] Jenna M. Drummond,[2] Greg G. Goss,[2,3] Jonathan G. C. Veinot[1,3]*

[1] Department of Chemistry, University of Alberta, 11227 Saskatchewan Drive, Edmonton, Alberta, Canada. E-mail: jveinot@ualberta.ca; Fax: +1-780-492-8231; Tel: +1-780-492-7206
[2] Department of Biological Sciences, University of Alberta, Edmonton, Alberta T6G2E9
[3] University of Alberta/National Research Council of Canada Nanotechnology Initiative

 # these authors contributed equally to this work

*** Corresponding author**

ABSTRACT

The design and fabrication of Si-based multi-functional nanomaterials for biological and biomedical applications is an active area of research. The potential benefits of using Si-based nanomaterials are not only due to their size/surface-dependent optical responses but also the high biocompatibility and low-toxicity of silicon itself. Combining these characteristics with the magnetic properties of Fe_3O_4 nanoparticles (NPs) multiplies the options available for real-world applications. In the current study, biocompatible magnetofluorescent nano-hybrids have been prepared by covalent linking of Si quantum dots to water-dispersible Fe_3O_4 NPs *via* dicyclohexylcarbodiimide (DCC) coupling. We explore some of the properties of these

magnetofluorescent nano-hybrids as well as evaluate uptake, the potential for cellular toxicity, and the induction of acute cellular oxidative stress in a mast cells-like cell line (RBL-2H3) by heat induction through short-term radio frequency modulation (10 min @ 156 kHz, 500 A). We found that the NPs were internalized readily by the cells and also penetrated the nuclear membrane. Radio frequency activated nano-hybrids also had significantly increased cell death where > 50% of the RBL-2H3 cells were found to be in an apoptotic or necrotic state, and that this was attributable to increased triggering of oxidative cell stress mechanisms.

INTRODUCTION

Bringing together materials with complementary properties to form bonded hybrids can lead to predicted, as well as unforeseen characteristics that hold the promise of broad impacts that reach beyond those of the isolated constituents.[1,2] One particularly appealing combination sees light emission and magnetism brought together to provide materials with enhanced functionality.[3–10] In each of these cases, a fluorescent cell imaging agent rendered responsive to an externally applied magnetic field could offer the possibility of simultaneous detection and separation of targeted cell populations and has the potential to be exploited as a therapeutic.[4,6,11]

An array of quantum dot (QD)-based magnetofluorescent probes have been reported; they are typically prepared by linking prototypical CdSe quantum dots (QDs) with magnetic nanoparticles (NPs) using various approaches including high-temperature decomposition,[12] doping,[13] crosslinking,[14] encapsulation,[15] leading to the formation of nanocomposites.[16] Bawendi et al. prepared what they coined “super-NPs” via the co-assembly of Fe_3O_4 NPs ‘core’ with a ‘shell’ of fluorescent CdSe@CdS QDs.[17] Following assembly, they introduced a silica layer that stabilized

the assemblies, provided a platform for surface functionalization, as well as improved biocompatibility.[17] These super-NPs were subsequently used as a dual-mode probe for *in vivo* imaging.[17] Despite offering important proof-of-concept advances, widespread real-world biological/medical application of most metal-based QDs (i.e., CdSe) is extremely unlikely due to the high inherent toxicity of Cd.[18]

The promise of a biologically compatible magnetofluorescent probe was recently highlighted in a review by Marcelo *et al*.[19] Nanomaterials based upon Group 14 elements, most prominently silicon QDs, offer all of the benefits (e.g., tunable surface chemistry and photoluminescence, *etc*.[20–23] of heavy-metal containing QDs, while also being biocompatible.[24,25] Not surprisingly, Si-based magnetofluorescent labels have been prepared and investigated, although to a far lesser extent than those based on other QDs. Swihart *et al.* developed a magnetofluorescent probe by encapsulating hydrophobic SiNPs and Fe_3O_4 NPs in phospholipid-polyethylene glycol micelles.[10] These hydrophilic micelles have a hydrophobic core of NPs and were used for *in vitro* and *in vivo* bio-imaging.[10] In another study, Sailor *et al.* fabricated luminescent microparticles made of porous-Si and loaded with Fe_3O_4 NPs and the anti-cancer drug doxorubicin to target-deliver the drug to human cervical cancer cells *in vitro*.[31] However, there are some concerns with this therapeutic formulation due to bio-incompatibility and inherent toxicity of hydrophobic Fe_3O_4 NPs.[26,27]

The magnetic response of iron oxide-containing NPs makes them intriguing for medical applications as they can act as an MRI contrast agent. While their application as contrast agents has been well documented and explored,[28–33] a less widely known property of iron oxide-containing NPs is the ability to inductively heat when placed in a modulating magnetic field. The

inductive heating effect of iron oxide NPs was first demonstrated over 60 years ago (1957), but they have only recently been promoted for clinical applications.[34,35] Current research primarily focuses on the optimization of iron oxide nanomaterials toward magnetohyperthermia and making the material more suitable for multimodal medical applications.[36–39] This promising approach capitalizes on external stimuli to induce cell apoptosis/necrosis, similar to light-based therapies. However, radio frequency (RF) modulation has the advantage of deeper tissue penetration (cm vs. mm for photo-induced hyperthermia).[40] A drawback of inductive heating is the limitation of lower heating efficiency, thus requiring higher NP concentrations to induce apoptosis/necrosis.[40]

Iron oxide NPs have been combined with various other nanomaterials to produce dynamic therapeutic platforms.[40,41] This includes combining with gold NPs to marry the photo and magneto induced hyperthermia of these two materials to yield a synergistic heating effect.[40] Similarly, iron oxide/SiO_2 core/shell NPs have been conjugated with CdSe/ZnS quantum dots to make luminescent magnetic hybrids.[41] While these aforementioned luminescent hybrids are effective, killing 99.2% of pancreatic human cancer cells after 2 min using a dose of 1.66 µg/ml, [41] these materials use the toxic/restricted metals discussed above, resulting in severe and uncontrolled non-target effects that limit their practical application in clinical settings.

In this study, we have combined the optical properties (i.e., visible photoluminescence) of SiQDs with the magnetic response of hydrophilic Fe_3O_4 NPs by covalently linking these materials. Herein, a water-dispersible magnetic-photoluminescent hybrid material has been synthesized *via* DCC coupling of acid-functionalized SiQDs and hydrophilic amine-terminated magnetite (Fe_3O_4) NPs. Moreover, its cytotoxicity and application as a theranostic agent (i.e., cell-

imaging and magneto hyperthermia) were studied and demonstrated using the rat basophilic leukemia (RBL)-2H3 cell line. RBL-2H3 cells are mast cell-like immune cells and are a commonly used cell model for the examination of immune system responses to foreign agents, such as allergens and other contaminants, including NPs.[42–46] Mast cells are located at the interface between the internal and external environments in the mucosal linings of the respiratory and gastrointestinal tracts, in blood vessels and in the skin, where they monitor for potential non-self antigens to target and remove. The primary immune function of mast cells is degranulation, a receptor-mediated effector response in which vesicle-stored antimicrobial and inflammatory granules (e.g., histamine) are released in an attempt to destroy foreign antigens.[47] RBL-2H3 cells can also internalize particles using various uptake mechanisms such as phagocytosis.[48] Therefore, since mast cells are early detectors of foreign particles and are likely to encounter infiltrated and circulating NPs, they are ideal cell candidates for determining the biocompatibility of novel NPs.

RESULTS AND DISCUSSION

Prevailing methods for preparing monodispersed Fe_3O_4 NPs are based on the thermal decomposition of iron precursors in the presence of different surfactants and capping agents such as oleic acid and oleylamine.[49–52] Although these approaches yield a narrow size distribution of magnetite NPs, the bio-incompatibility, toxicity, and hydrophobicity of the final Fe_3O_4 particles limit their use for biological imaging and other biomedical purposes.[26,53] We have chosen to employ an alternative approach involving the microwave-assisted *in-situ* hydrothermal synthesis and functionalization of Fe_3O_4 NPs in the presence of excess capping agent (e.g., (3-aminopropyl)trimethoxysilane, APTMS).[5,7,26,53–56] The resulting APTMS-capped magnetite NPs

form a uniform suspension in water that can be attracted to an external magnetic field (Figure 1a).

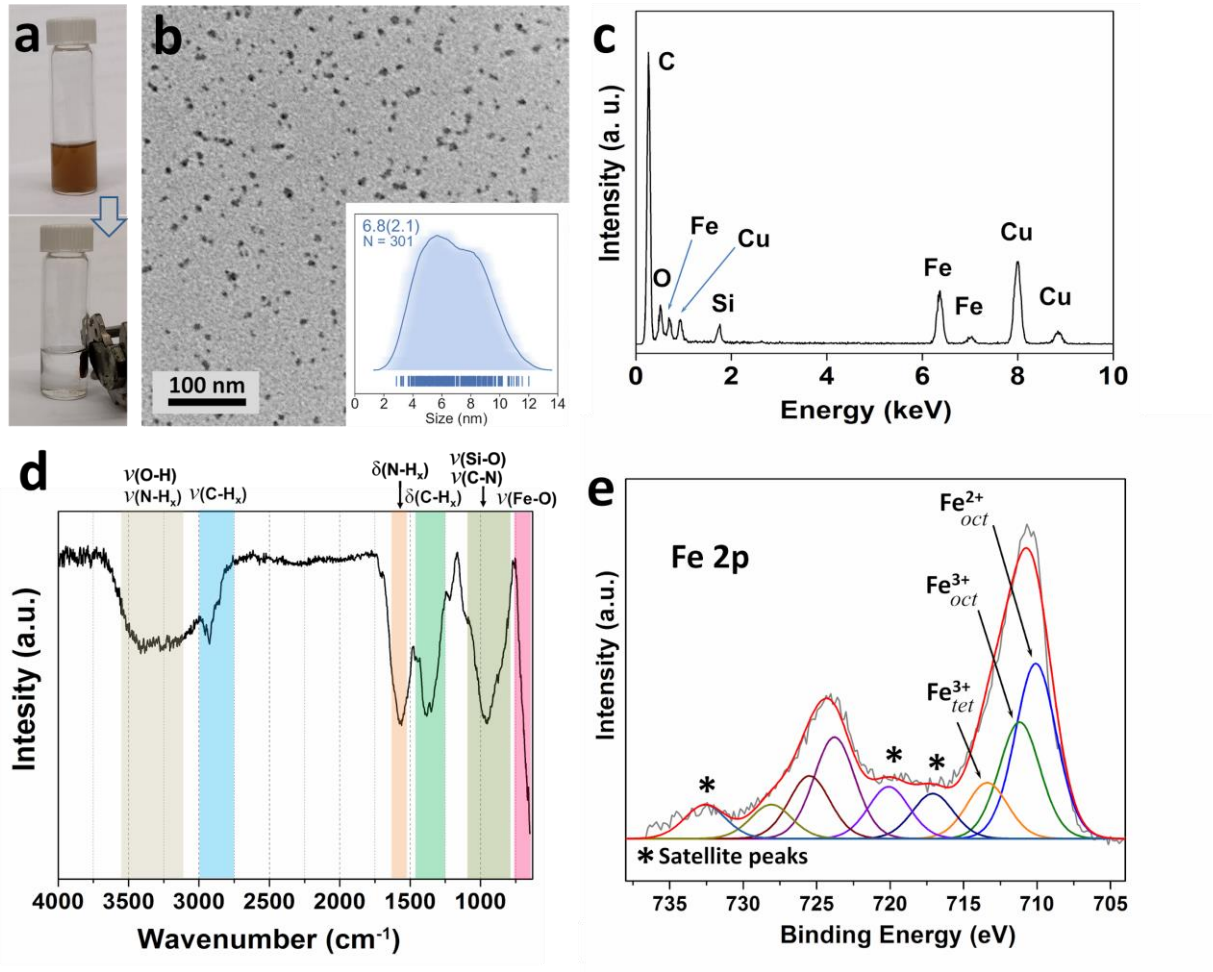

Figure 1. Characterization of APTMS-capped Fe_3O_4 NPs: a) A photograph of a water dispersion of APTMS-capped Fe_3O_4 before (left) and after (right) exposure to a permanent magnet. b) A representative bright-field TEM image (Inset: Average-shifted histogram showing an average diameter = 6.8 ± 2.1 nm). c) EDX, d) FT-IR spectra, and e) The Fe 2p region of the high-resolution XP spectrum with appropriate fitting for Fe^{2+} and Fe^{3+}.[57–62]

TEM analyses of APTMS-capped magnetite particles (Figures 1b and S1 in Supplementary Information) show NPs with a size distribution of 6.8 ± 2.1 nm (Figure 1b). NPs of this size are

considerably smaller than the single-domain dimension of bulk Fe_3O_4 (i.e., 128 nm)[63,64] and are known to exhibit superparamagnetic behavior.[65] Superparamagnetic particles have no coercivity; hence they will not remain aggregated and freely demagnetize and reorient after removing the magnetic field.[65] HRTEM imaging (Figure S1) shows lattice fringes of 0.29 nm that correspond to the {220} planes of bulk Fe_3O_4.[66] The EDX spectrum of APTMS-capped Fe_3O_4 NPs (Figure 1 c) indicates the presence of iron, oxygen, silicon, and carbon at the sensitivity of the method (± 1-2% atomic % depending on Z).[67]

The IR spectrum of APTMS-capped Fe_3O_4 NPs (Figure 1d) shows broad and strong absorption from N-H stretching of the amine functionality at ca. 3410 cm^{-1} along with corresponding bending at *ca.* 1580 cm^{-1}. Features associated with aliphatic C-H stretching and bending are noted at 2960 and 1400 cm^{-1}, respectively. In addition, features associated with Si-O (*ca.* 1130 cm^{-1}) and strong Fe-O stretching (ca. 650 cm^{-1}) provide further evidence of APTMS functionalization of the magnetite NP surface.[68–70] The XP survey spectrum of magnetite NPs (Figure S2) exhibits the expected features arising from Fe_3O_4.[57–61] Figure 1e shows a high-resolution XPS of Fe 2p spectral region; three features at binding energies of 710.5, 712.1, and 713.7 eV, corresponding to Fe^{2+}, Fe^{3+} octahedral, and Fe^{3+} tetrahedral. Two other features at 717.6 and 720.7 eV are related to satellite peaks for Fe^{2+} and Fe^{3+} are also noted.[62]

SiQDs were prepared by the method developed in the Veinot lab that involves the reductive thermal processing of hydrogen silsesquioxane.[71] For the present study, hydride-terminated SiQDs liberated from the oxide matrix upon HF etching were functionalized with undecanoic acid moieties using an established radical-initiated surface hydrosilylation protocol.[72]

Brightfield TEM imaging of undecanoic acid-functionalized SiQDs (Figure 2a) shows pseudospherical SiQDs and a size distribution of 4.6 ± 0.8 nm (Figure 2a, inset), while HRTEM analysis (Figure 2c) shows fringes of 0.33 nm, characteristic of the Si {111} lattice spacing. Furthermore, EDX analysis indicates that the functionalized SiQDs are expectedly composed of silicon, carbon, and oxygen (Figure 2b). Consistent with previous reports, the photoluminescence spectrum of SiQDs of these dimensions shows an emission maximum at *ca.* 720 nm upon excitation at 350 nm (Figure 2d and e).[73] The FT-IR spectrum (Figure 2f) clearly shows characteristic features related to surface bonded 10-undecanoic acid (i.e., O-H stretching *ca.* 3400 cm^{-1}, C-H stretching *ca.* 2900 cm^{-1}, C-H bending *ca.* 1400, C=O stretching *ca.* 1708 cm^{-1}).

We also note evidence of residual Si-H stretching at *ca.* 2100 cm^{-1} and Si-O-Si at *ca.* 1100 cm^{-1}. The survey XP spectrum of undecanoic acid-functionalized SiQDs (Figure S3) exhibits the expected features arising from SiQDs. At the same time, the high-resolution scan of the Si spectral region (Figure 2g) is consistent with the present EDX and IR analysis suggesting some surface oxidation.

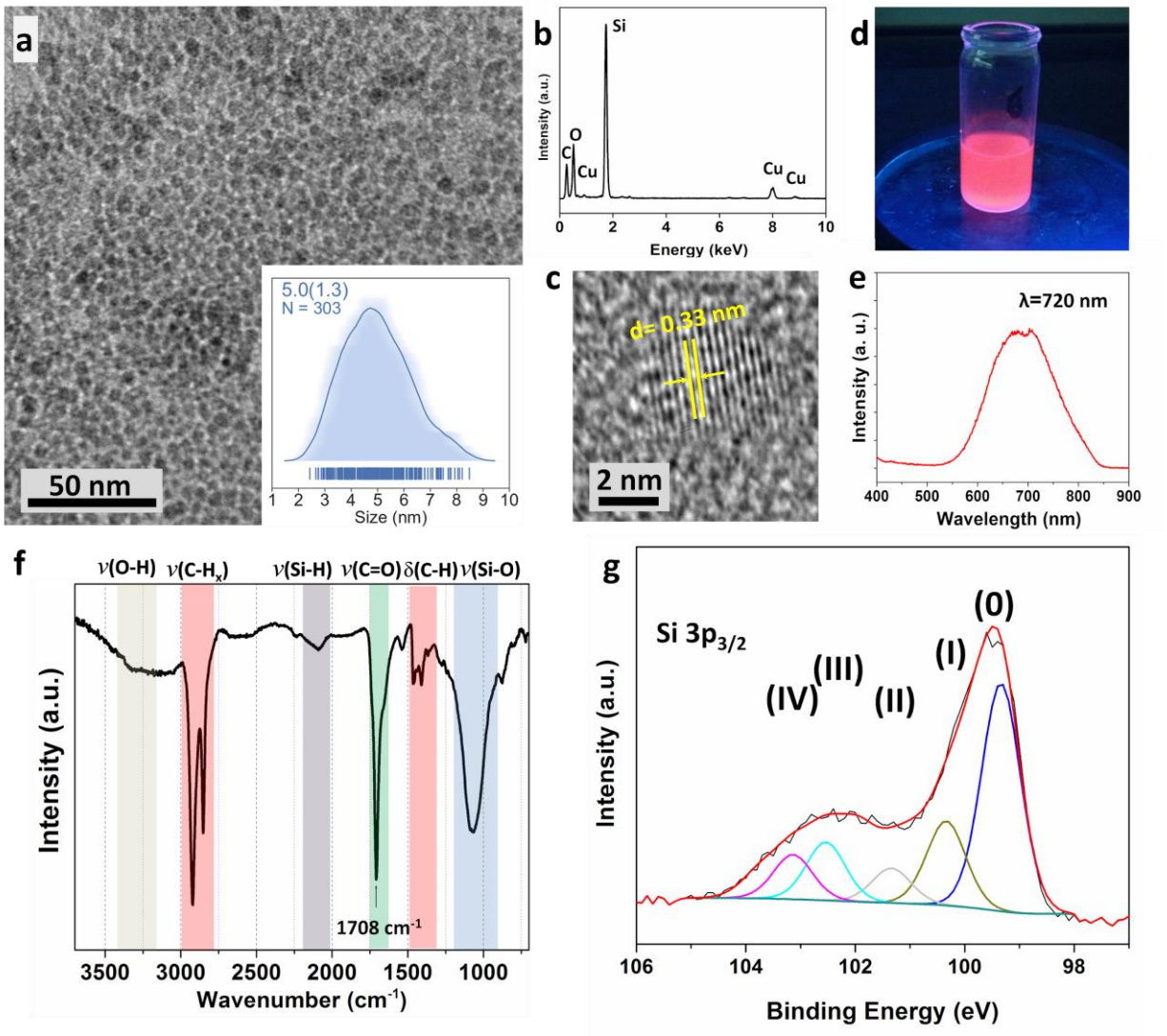

Figure 2. a) Bright-field TEM image and size distribution of undecanoic acid-functionalized SiQDs. b) EDX spectrum of undecanoic acid-functionalized SiQDs. c) HRTEM image of a representative SiQDs showing lattice fringes arising from Si [111] planes. d) A photograph of a water dispersion of undecanoic acid-functionalized SiQDs under 350 nm illumination. E) PL spectrum upon excitation at 350 nm. f) FT-IR spectrum. g) Si 2p region of the high-resolution XP spectra of undecanoic acid-functionalized SiQDs showing fitting for the Si $2p_{3/2}$ component. (The Si $2p_{1/2}$ components have been omitted for clarity.)

With the development of APTMS-capped magnetite and undecanoic acid-functionalized SiQDs, the coupling of these two functional components was achieved using established

dicyclohexylcarbodiimide (DCC) mediated coupling (Scheme 1).[74–76] Carboxylic acid-terminated SiQDs were first activated with DCC and subsequently exposed to amine-terminated Fe_3O_4 NPs to form amides linkages. The resulting hybrids were freed from reaction byproducts (e.g., carboxylic acid anhydride, N,N'-dicyclohexylurea) and uncoupled SiQDs, upon repeated isolation by magnetic separation/re-dispersion cycles.

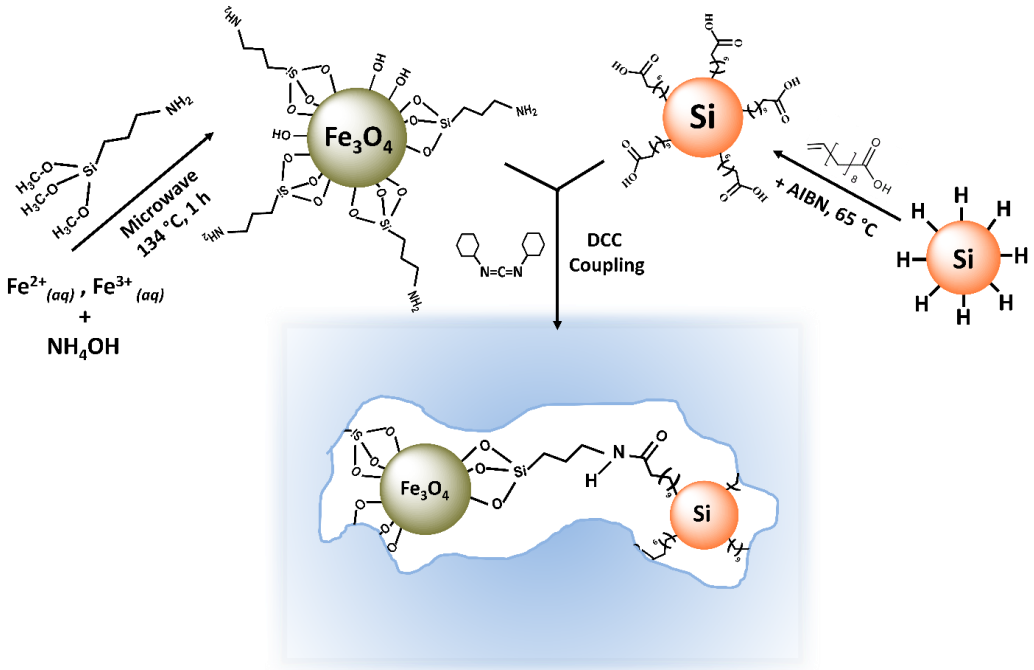

Scheme 1. Synthesis of Si-amide-Fe_3O_4 NPs via DCC coupling of undecanoic acid-terminated SiQDs and APTMS-capped Fe_3O_4 NPs

Figure 3a (as well as video S1 in SI) illustrates water dispersed Si-amide-Fe_3O_4 NPs exposed to a benchtop UV light before, during, and after exposure to a permanent magnet. Qualitative inspection immediately reveals the Si-amide-Fe_3O_4 NPs retain the SiQD optical response, which is also manifested in the PL spectrum (Figure 3b) that shows no shift in the PL maximum after the coupling reaction. The response of the Si-amide-Fe_3O_4 NPs upon exposure to a permanent magnet also provides a qualitative indication of coupling as the hybrid particles are attracted to

the magnet. Infra-red spectroscopy (Figure S4) further confirms covalent coupling of carboxylic acid-functionalized SiQDs with amine termination of APTMS-capped Fe_3O_4 NPs and shows features characteristic of the constituent SiQD and Fe_3O_4 NP components, as well as the expected amide linkage (i.e., amide carbonyl stretching at 1643 cm^{-1}).

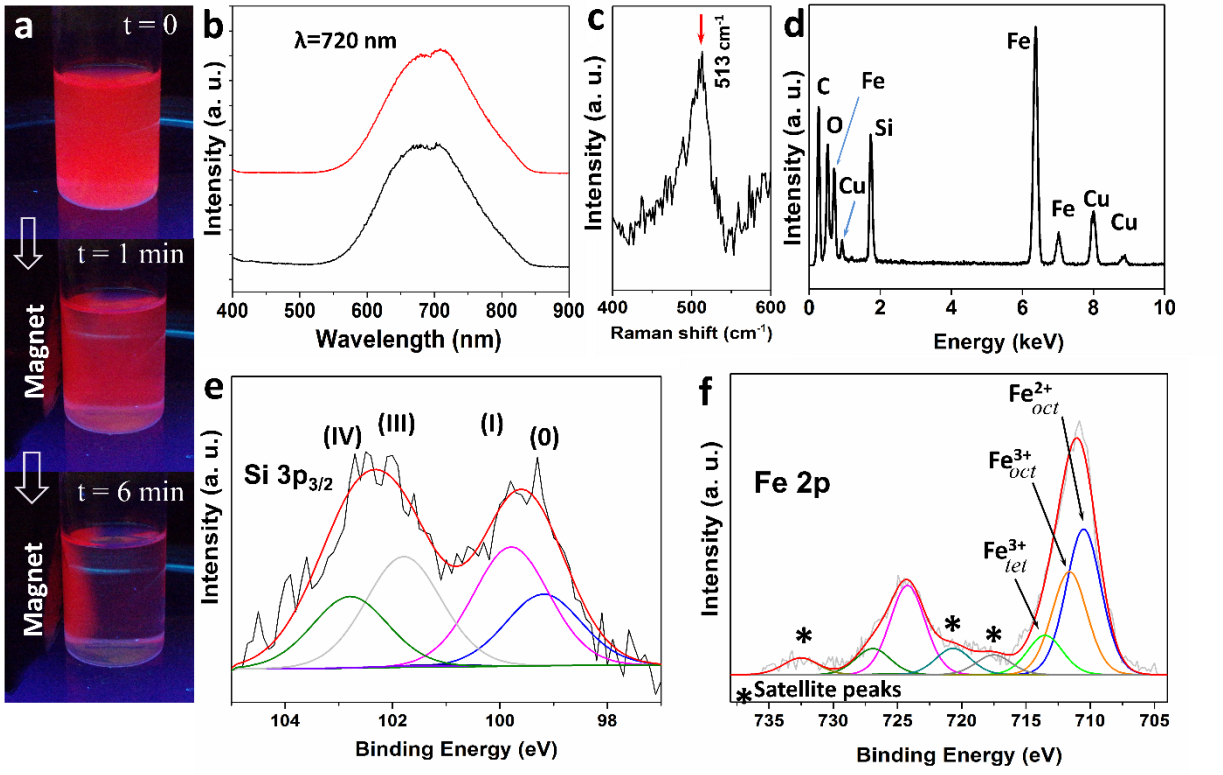

Figure 3. a) A photograph of water suspended Si-amide-Fe_3O_4 NPs (*ca.* 1 mg/mL) upon exposure to a benchtop UV light and a permanent magnet. b) PL spectra of SiQDs (black trace) and Si-amide-Fe_3O_4 NPs (red trace) upon excitation at 350 nm. c) Raman spectrum of Si-amide-Fe_3O_4 nano-hybrids. d) EDX spectrum of Si-amide-Fe_3O_4 nano-hybrids. e, f) Si 2p and Fe 2p regions of high-resolution XP spectra Si-amide-Fe_3O_4 nano-hybrids.

Raman spectroscopy shows a feature at 523 cm^{-1} indicative of Si-Si bonding, which is consistent with the SiQD integrity being maintained during coupling. EDX (Figure 3d) and XP spectroscopy (Figure S5) confirm the presence of carbon, oxygen, iron, and silicon. Furthermore,

the high-resolution XP of the Si spectral region (Figure 3e) shows emissions associated with Si(0) as well as Si sub-oxides, and the Fe region (Figure 3f) confirms the presence of Fe_3O_4 (*vide supra*). Figure S6 also shows several bright-field TEM images of Si-amide-Fe_3O_4 nano-hybrids. The aggregated structures shown in these images confirm that several Fe_3O_4 NPs (darker spots) were attached to SiQDs (lighter spots). Higher contrast TEM images, as well as elemental mapping analysis, was not possible due to the thick layer of different ligands (e.g., undecenoic acid, APTMS, coupled amide moieties) on the surface of Si-amide-Fe_3O_4 nano-hybrids.

Following the development of stable, magnetic, and photoluminescent Si-amide-Fe_3O_4 nano-hybrid NPs, our next objective was to investigate their biocompatibility by measuring the effects of Si-amide-Fe_3O_4 NP exposure on RBL-2H3 cell viability and functionality at a range of doses. Results from these tests showed that after 1 h of *in vitro* exposure, Si-amide-Fe_3O_4 NPs did not increase apoptosis in RBL-2H3 cells in all doses aside from the highest tested (i.e., 100 μg/mL). Under those conditions, the percentage of necrotic cells increased significantly (8.2 ± 0.74 % SEM) compared to the other doses, including the control (1.8 ± 0.17%) (Figure 4**).** After a 24 h exposure, the percentage of late apoptotic (0.1 μg/mL: 14.7 ± 2.1%, 1 μg/mL: 13.3 ± 1.2%, 10 μg/mL: 12.8 ± 1.0%, 100 μg/mL: 12.7 ± 1.2%) and necrotic (0.1 μg/mL: 10.9 ± 2.3%, 1 μg/mL: 12.2 ± 0.5%, 10 μg/mL: 10.9 ± 1.1%, 100 μg/mL: 16.8 ± 1.5% SEM) cells increased (approximately doubling) in all the tested NP doses when compared to vehicle control (6.9 ± 0.4% SEM), but with no difference in the percent increase of late apoptotic and necrotic cells for any of the doses (Figure 4). Despite some decreases in cell viability, when cell death is normalized to vehicle controls over 24 h, the percentage of dead and dying cells in the treatment groups drops to 5-10 % of the cell population. In this context, these results indicate that over a wide range of Si-amide-Fe_3O_4 NP doses, only a

very small number of RBL-2H3 cells are adversely sensitive to Si-amide-Fe_3O_4 NPs, and only after 24 h. Furthermore, given that immune mast cells actively interact with foreign particles and are located at mucosal boundaries with the external environment, means they are likely key targets for NPs and could be increasingly prone to toxicity. Therefore, these low levels of cell death under controlled conditions indicate that these Si-amide-Fe_3O_4 NPs are likely highly biocompatible. Moreover, the immunological response of RBL-2H3 cells towards the Si-amide-Fe_3O_4 NPs showed that at low doses these cells do not significantly degranulate as measured by the β-hexosaminidase (β-hex) release assay (Figure S7), while at the highest dose, only a small immune response was triggered, further indicating biocompatibility of the Si-amide-Fe_3O_4 NPs toward highly sentinel immune cells. These results are in contrast to other NPs that show potent immune degranulatory stimulation in RBL-2H3 cells when exposed to metal[77] and non-metal based NPs.[46]

Previous biocompatibility studies have shown that cell death from Fe-based NPs is attributed to oxidative stress from the generation of reactive oxygen species (ROS) when NPs act as catalysts in Fenton reactions.[78] Free radical toxicity is a common mechanism by which many types of NPs can affect cell health, and excessive ROS products can initiate cellular apoptosis by causing excessive damage or changes to the cytoplasmic and/or inner mitochondrial membranes.[79,80] Mitochondrial destabilization results in the loss of mitochondrial transmembrane potential and the downstream activation of the proteolytic caspase cascade that lead to the execution pathway and the final death of the cell.[81] The increase in late apoptosis of a small population of cells after 24 h suggests that these NPs are activating the caspase cascade, likely through the intrinsic apoptotic pathway, which is a known target for free radicals, and are not causing cell death via necrosis, a distinct modality for cell death.[82,83]

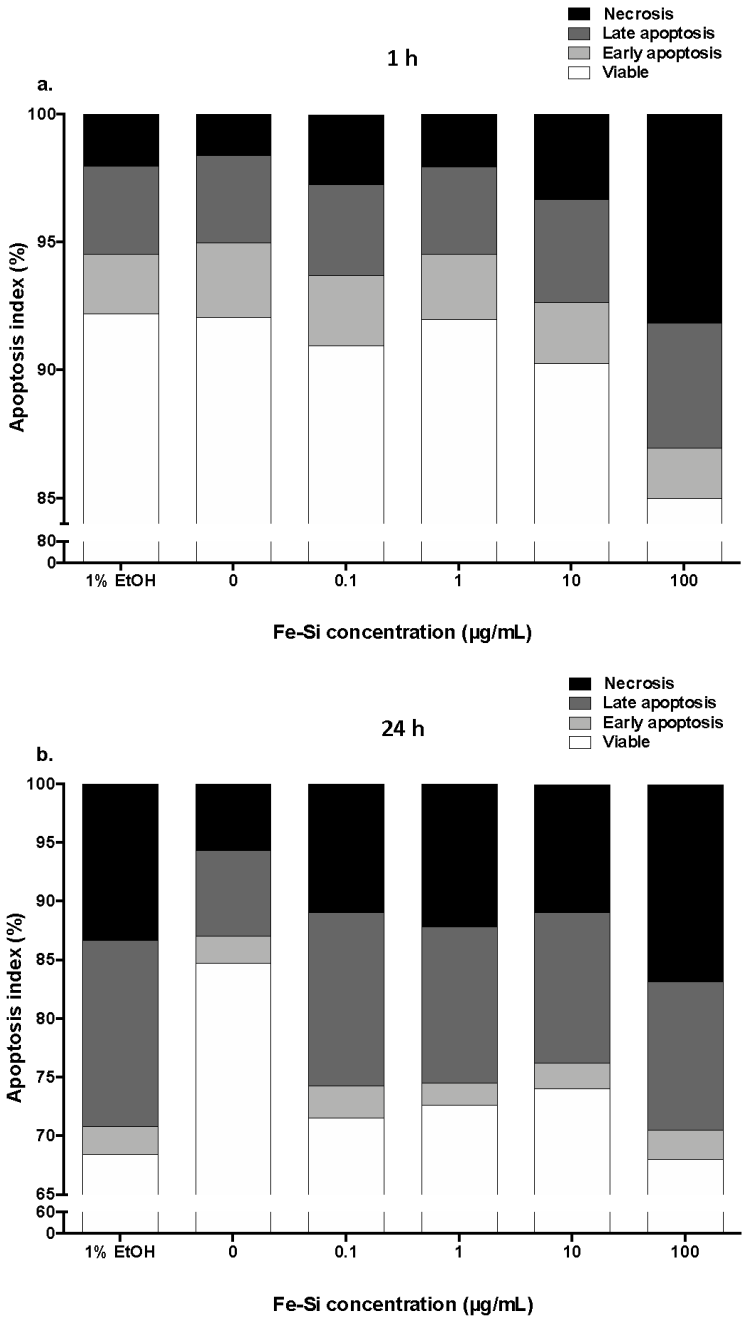

Figure 4. Cellular apoptosis results of RBL-2H3 cells following exposure to 0 (PBS, vehicle control), 0.1, 1, 10, 100 µg/mL Si-amide-Fe_3O_4 NPs, plus1% ethanol (positive control) for (a) 1 h or (b) 24 h. Apoptosis is proportioned into: viable, early apoptosis, late apoptosis and necrosis cell death categories for each exposure period. Data are means ± SEM n = 5 independent experiments. Statistics are presented in Figure S8 and S9, where different lower-case letters denote significant differences (two-way ANOVA, $p<0.05$) within a cell death category, followed by a Tukey's pairwise multiple comparison test.

RBL-2H3 cells significantly internalized Si-amide-Fe_3O_4 NPs across a range of NP doses (Figure 5). Three-dimensional computer surface rendering of confocal images also confirmed that the NPs had penetrated the plasma membrane and were located mostly in the cytosol, but were also clearly observed inside the nucleus of RBL-2H3 cells (Figure 6 and Supplementary Animation S1 and Animation S2). The amount of NPs that penetrated the cells also increased dose-dependently. In a recent paper from our group, we also demonstrated that small NPs (<10 nm in size) were also readily taken up by blood endothelial cells using an ex vivo prep, with a percentage of NPs capable of penetrating through two cell layers into the vascular smooth muscle layer of the vessel walls.[77] The mechanism by which these NPs can enter cells is unknown. However, recent studies have suggested that clathrin receptor-mediated endocytosis is a primary internalization pathway by which NPs can penetrate the plasma membrane.[84] We have also recently shown that when clathrin receptors are pharmacologically antagonized, there is a significant reduction in the amount of NPs that are taken up by the cell,[77] suggesting that clathrin-mediated endocytosis is the dominant operative pathway for NP internalization.

From a biocompatibility perspective, the ability to regulate the number of NPs that can penetrate a cell presents an interesting opportunity to develop therapeutic NPs that can target various components of the cell. However, uptake into cells may also exacerbate cell death by mechanisms described above, and several reports correlate NP uptake and cell death.[45,85] The increased percentage of late apoptotic cells after a 24 h exposure to the highest NP dose (100 μg/mL) may be partially explained by the increased uptake of Si-amide-Fe_3O_4 NPs. Their internal

presence may increase the amount of ROS that are generated and trigger apoptotic pathways in the cell.

The uptake of the Si-amide-Fe_3O_4 NPs by the nucleus is of particular interest as it is not common for nanomaterials to enter the cell nucleus.[86,87] While carbon-based nanomaterials (MWCNT, graphene/carbon quantum dots, and C60) will enter the cell nucleus without additional modification, most other nanomaterials require an additional nuclear localization sequence peptide (NLS) tagged to the surface of the nanomaterial to facilitate the crossing of the nuclear envelope.[87–89] Previously it has been shown that small CdTe QDs (2.2 nm; green photoluminescence) localize primarily in the nucleus, while larger CdTe QDs (5.2 nm; red photoluminescence) were localized primarily in the cytoplasm. It is particularly desirable to get red-emitting QDs into the nucleus without the use of an NLS.[90,91] Entry into the cell nucleus is typically limited to small NPs (<5 nm) and can be extended to 20 nm by employing an NLS peptide to assist with passage through the nuclear envelope.[92] Iron oxide NPs, in particular, tend to remain in the perinuclear region without further modification.[93,94] Our magnetofluorescent nano-hybrids cross both the cell and nucleus membranes without a need for an NLS tag, thus overcoming typical limitations of nanomaterials for nuclear targeting.[95] This important finding suggests the present NP systems could be used for gene and drug delivery applications without requiring an additional transport agent (such as NLS).[95]

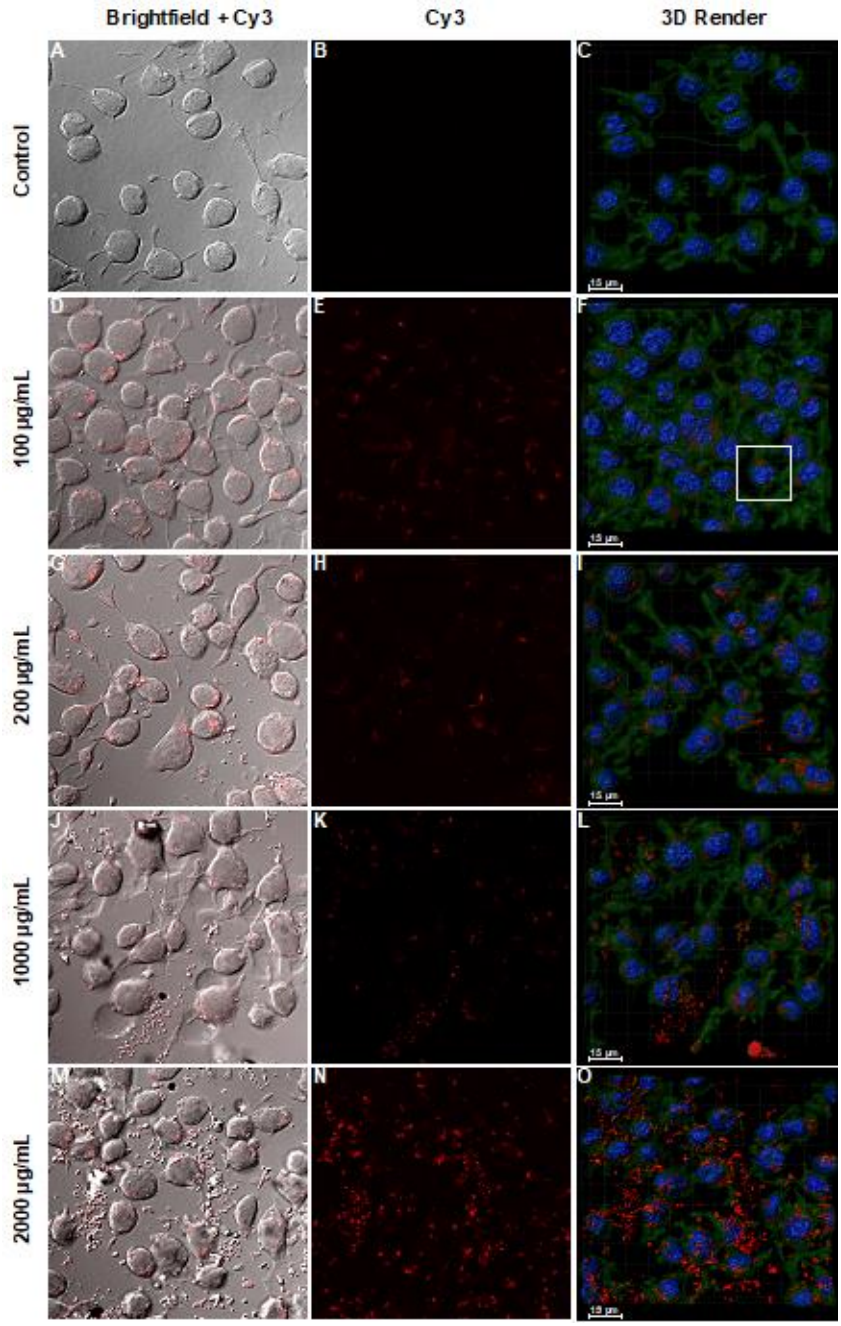

Figure 5. Confocal microscopy (Objective 40x, 1.3 oil plan-Apochromat) images of RBL-2H3 cells following exposure to 0, 100, 200, 1000 and 2000 µg/mL Si-amide-Fe_3O_4 NPs for 1 h. Representative bright field optical micrographs after differential interference contrast (A, D, G, J, M), Cy3 (i.e., red NPs) fluorescence micrographs (B, E, H, K, N) and three-dimensional surface rendering of cells (C, F, I, L, O). DAPI (Blue) and FITC (Green; 75% transparent surface for three-dimensional reconstruction) were used as probes for cell nucleus and plasma membrane, respectively. Scale bars for three-dimensional images are 15 µm, respectively. The cell within white inset box on panel F was selected for single-cell three-dimensional rendering in Figure 6.

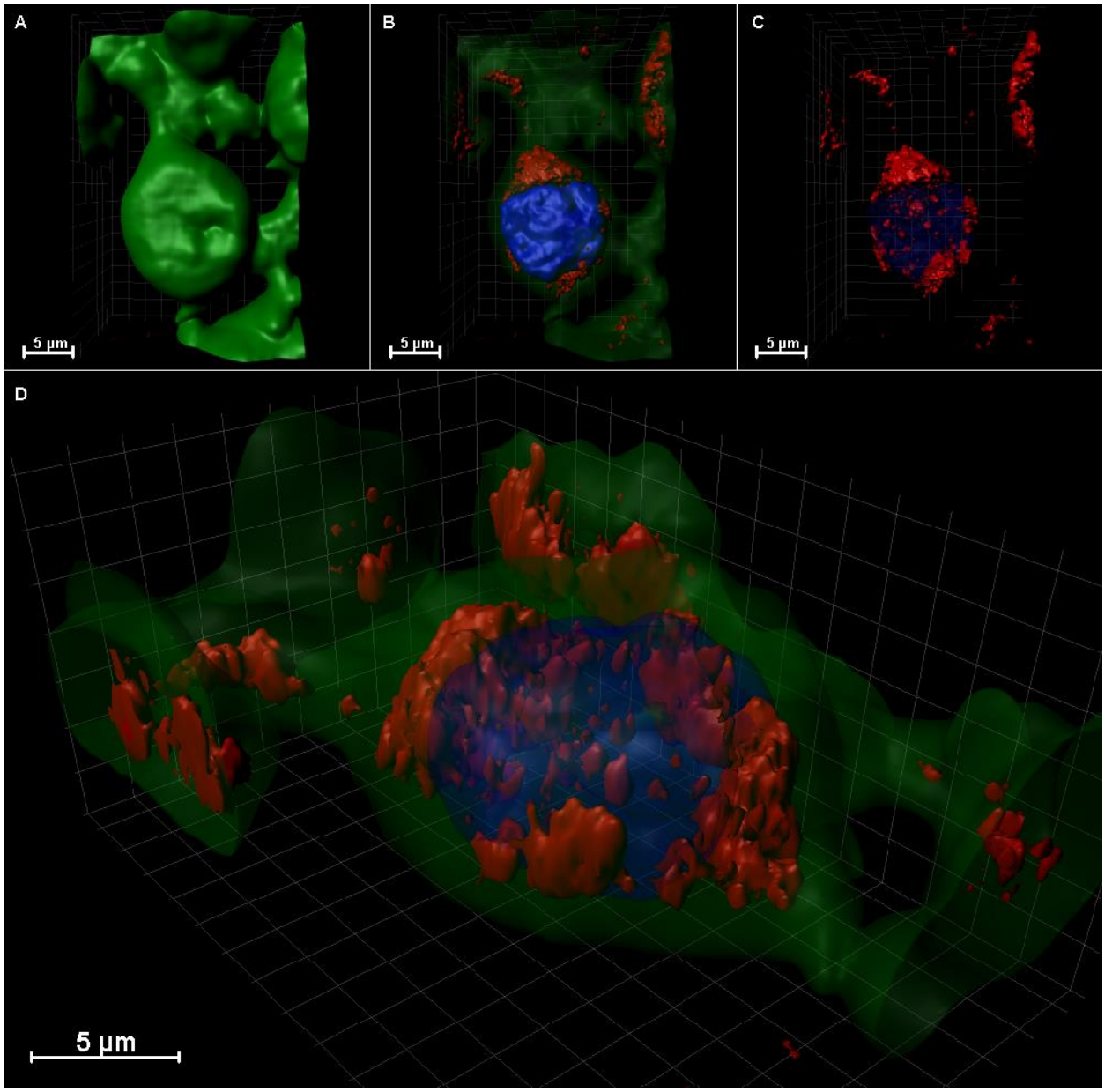

Figure 6. Three-dimensional surface rendering of a representative RBL-2H3 cell following exposure to 100 µg/mL Si-amide-Fe_3O_4 NPs (Cy3 red fluorescence) for 1 h. DAPI (Blue) and FITC (Green) were used as probes for cell nucleus and plasma membrane, respectively. (A) Cell with non-transparent plasma membrane, (B) cell with 75% transparent plasma membrane, (C) cell with 100% transparent plasma membrane and 75% transparent nucleus and (D) cell positioned horizontally with 75% transparent plasma membrane and 75% transparent nucleus, clearly show penetration of Si-amide-Fe_3O_4 NPs inside the plasma and nuclear membranes. Scale bars for three-dimensional images are 5 µm, respectively. Animated movies (Animation S1 and S2) can be found in the Supplemental material.

With the knowledge that Si-amide-Fe_3O_4 NPs are readily internalized by the cells, we tested their potential use in inductive heating to induce apoptosis/necrosis. The effect of the radio-frequency (RF) treatment is detected with Si-amide-Fe_3O_4 NP doses as low as 10 μg/mL and RF treatments of 100 A (222 W, 159 kHz) for 1 min. The impact of RF treatment increases with increasing current, time, and concentration of Si-amide-Fe_3O_4 NPs (Figure 7). The maximum effect can be seen with a concentration of 100 μg/mL and an RF treatment of 500 A (3984 W, 156 kHz) for 10 min. When the cells in PBS buffer were exposed to RF treatment without NPs, they were not significantly impacted indicating the effect arise from the combined presence of the Si-amide-Fe_3O_4 NPs and the RF treatment. The frequency and power settings used in the present study were significantly less than those proposed by Xu *et al*.[41] In our experimental design, the sample was set below the coil to minimize cell loss and disruption due to handling/transfer of the cells. Thus the magnitude of magnetic field experienced by the sample was likely less than that moving through the coil. This factor, combined with the lower frequency and power, accounts for why we only see ~50% of cells in early apoptosis, late apoptosis, or necrosis. Interestingly, we begin to observe cell death at 1/10 the power and half the frequency used by previous researchers.[41] At 156 kHz, the penetration depth will be greater than 25 cm, and significantly more than the 4-6 mm treatment depths reported for photodynamic therapy.[40,96]

To gain further insight into the mechanism leading to cell death, an oxidative stress assay was performed using the same experimental approach to determine the change in ROS formation upon exposure to an RF field. While heating of photothermal agents attached to Fe_2O_3 nanomaterials have shown an increase in ROS formation, this effect has not been shown for inductive heating of Fe_2O_3 NPs.[97,98] Cell exposure to the Si-amide-Fe_3O_4 NPs alone resulted in significant dose dependent increases in ROS from 0.1 to 100 μg/mL (Figure 8, Figure S10). The

particularly high levels of ROS-mediated oxidative stress at the highest dose (100 µg/mL) was likely the trigger that initiated increased apoptotic cell death in the same dose in Figure 4.

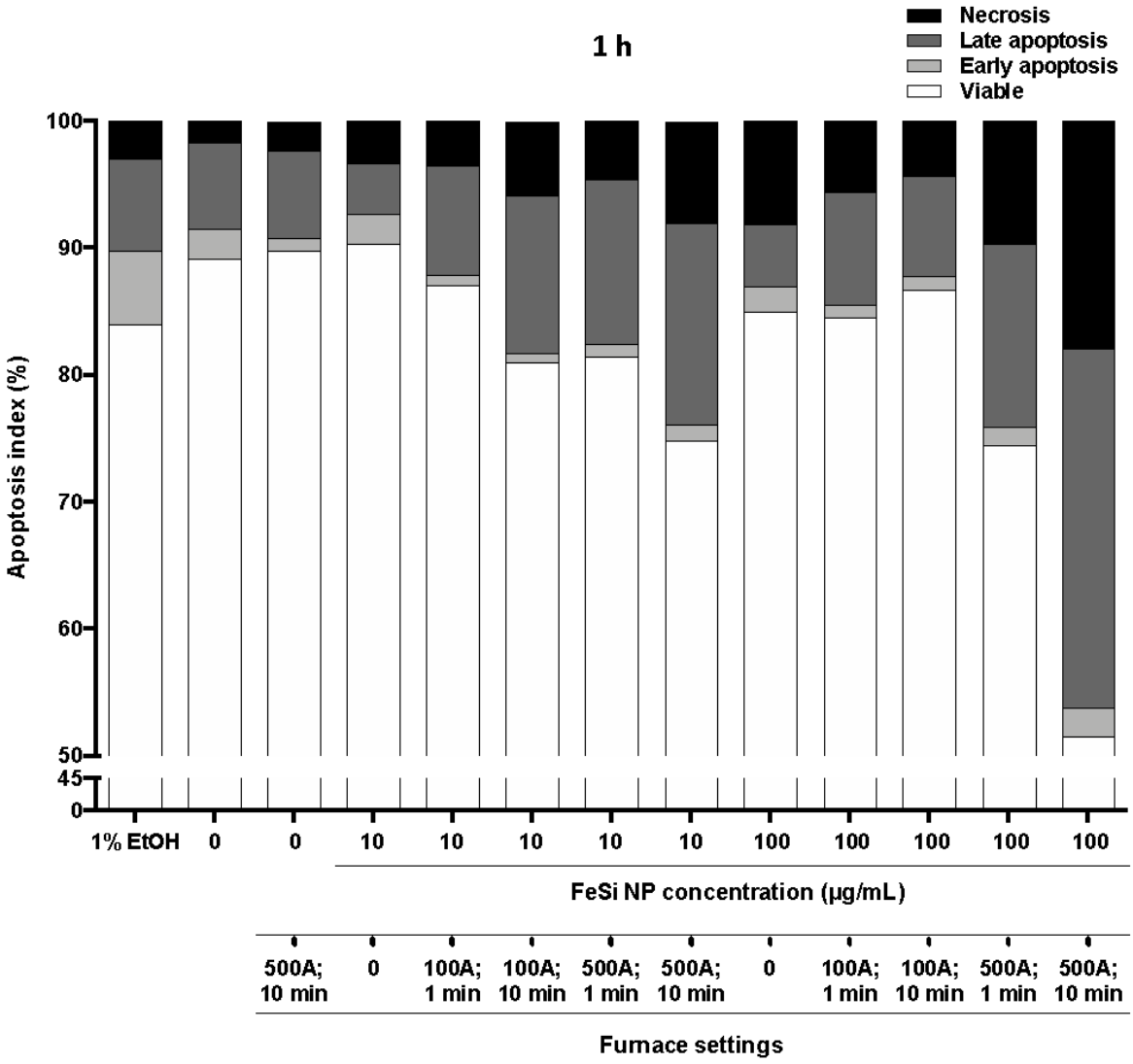

Figure 7. Cellular apoptosis results of RBL-2H3 cells exposed to 1% ethanol (positive control), or to 0 (PBS, vehicle control), 10 or 100 µg/mL Si-amide-Fe_3O_4 NPs for 1 h, followed by 1 or 10 min exposures to 100 or 500 A induction furnace heating settings. Apoptosis is proportioned into: viable, early apoptosis, late apoptosis and necrosis cell death categories as a histogram or into pie charts for each exposure period. Data are means ± SEM n = 5 independent experiments. Statistics are presented in Figure S11, where different lower-case letters denote significant differences (two-way ANOVA, $p<0.05$) within a cell death category, followed by a Tukey's pairwise multiple comparison test.

When cells were dosed with low concentrations (10 μg/mL) of Si-amide-Fe_3O_4 NPs and exposed to low inductive heating power (100 A), ROS formation increased significantly with longer exposure times (i.e. 1 min and 10 min) (Figure 8, Figure S10). This time-dependent increase in oxidative stress can be attributed to increasing Fenton reactions due to the minor heat generation of the Si-amide-Fe_3O_4 NPs upon exposure to an RF field. We also observed that the cellular ROS response was dependent on the combination of NP dose, heating power and time, whereby low dose (10 μg/mL) and higher power (500 A) produced less ROS than using lower power (100 A) (Figure S10). Excessively heating cells at the higher power may have resulted in quicker cell death and were thus less capable of producing ROS. When we used high dose (100 μg/mL) and high power (500 A), ROS generation was completely absent at both exposure times (1 and 10 min), suggesting that the cells may have immediately lysed and were not capable of producing ROS (Figure 8, Figure S10). Overall, the results from these experiments demonstrate that the mechanism of cell death can be precisely tuned by the concentration and power of the RF frequency that is applied, and that induction heating of biocompatible photoluminescent Si-amide-Fe_3O_4 NPs offer an attractive advancement for inducible hyperthermia in cells.

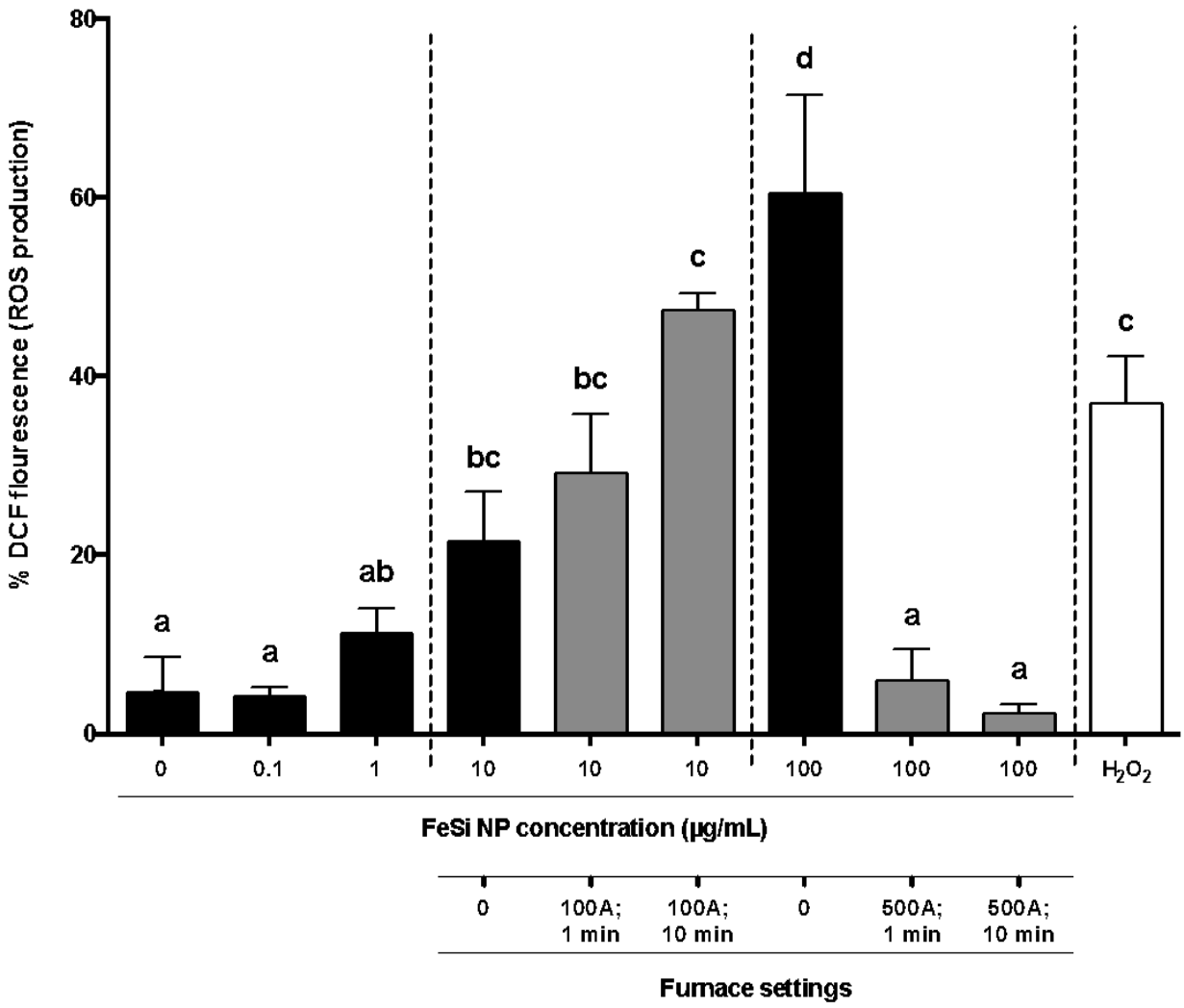

Figure 8: Cellular oxidative stress results of RBL-2H3 cells exposed to H_2O_2 (positive control, white bar, 30 min exposure) or to 0 (PBS, vehicle control), 0.1, 1, 10 and 100 µg/mL Si-amide-Fe_3O_4 NPs for 1 h (black bars), followed by 1 or 10 min exposures to 100 or 500 A furnace heating settings (grey bars). Data are means ± SEM n = 4-6 independent experiments. Different lower-case letters denote significant differences (one-way ANOVA, $p < 0.05$) between treatment groups, followed by a Tukey's pairwise multiple comparison test.

CONCLUSION

We have shown that nano-hybrids can effectively be prepared by covalent linking carboxylic acid-terminated SiQDs with amine-terminated Fe_3O_4 NPs via DCC coupling. The resulting nano-hybrids maintain the photoluminescence of the SiQDs and the magnetic response of the Fe_3O_4 NPs. These Si-amide-Fe_3O_4 NPs were also found to be mostly compatible with immune mast cell-like cells that actively engage with foreign materials. While there was a slight increase in apoptosis after a 24 h exposure period, the cell populations retained high levels of viability, especially when corrected for apoptosis in controls.

Using confocal imaging and 3D surface rendering, the Si-amide-Fe_3O_4 NPs were found to penetrate the plasma and nuclear membranes of RBL-2H3 cells. Uptake of other fluorescently-labeled NPs has been previously shown,[46,99,100] however, there are typically issues with bleaching and quenching of fluorescent signals, which can limit their time and the efficacy for visualizing tagged cells. As well, adding fluorescent molecules, such a FITC, to an engineered NP can change the physicochemical properties of that NP and interfere with its proposed use. Here, we have shown that Si-amide-Fe_3O_4 NPs can be used to label cells without altering their intended physicochemical properties, such as their fluorescence. This advantage provides better predictability for biological outcomes and allows developers to more easily modify specific NP properties if other intended uses are desired.

Finally, the internalized Si-amide-Fe_3O_4 NPs were exposed to an alternating magnetic field of varying power for either 1 minute or 10 minutes. It was shown that cell death can be induced and controlled based on the power, nano-hybrid concentration, and time of the exposure, where

the less power, lower concentrations, and shorter times lead to less cell death, and higher powers for longer times with higher concentrations increase cell death to almost 50%. This method can be complementary to photodynamic therapy where the heat change is significantly more, but the penetration depth is significantly less. This work enables future studies employing these biologically compatible magneto-fluorescent nano-hybrids for DNA testing, targeted cell death and multimodal imaging applications.

EXPERIMENTAL

Reagents and Materials. Hydrogen silsesquioxane (HSQ, trade name Fox-17, sold commercially as a solution in methyl isobutyl ketone) was obtained from Dow Corning Corp. (Midland, MI). Electronic grade hydrofluoric acid (HF, 49% aqueous solution) was purchased from J. T. Baker. Ferrous chloride tetrahydrate ($FeCl_2 \cdot 4H_2O$ > 99 %), Ammonium hydroxide (i.e., 29.3 wt % NH_3 in water), 10-undecenoic acid (98 %), 2,2'-azobis(2-methylpropionitrile) (AIBN, 98 %), (3-aminopropyl) trimethoxysilane (APTMS, 97 %), N,N'-dicyclohexylcarbodiimide (DCC, 99 %), as well as reagent grade of acetone, toluene, ethanol and methanol were purchased from Sigma-Aldrich. Toluene was dried using a Grubbs-type solvent purification system (Innovative Technologies, Inc.) prior to use. Ultrapure H_2O (18.2 MΩ/ cm) was obtained from a Barnstead Nanopure Diamond purification system and used in all reactions/manipulations involving water. Unless otherwise indicated, all reagents and solvents were used as received.

Material Characterization and Instrumentation. Fourier-Transform Infrared Spectroscopy (FT-IR) was performed using a Nicolet Magna 750 IR spectrophotometer. Samples were prepared by

drop-casting a solution/suspension containing material in question (ethanol, SiQDs; water, Fe_3O_4 NPs and Si-amide-Fe_3O_4) onto a Si wafer substrate. Transmission electron microscopy (TEM) and energy dispersive X-ray (EDX) analyses were performed using a JEOL-2010 (LaB6 filament) electron microscope with an accelerating voltage of 200 kV. High-resolution TEM (HRTEM) imaging was performed on JEOL-2200FS TEM instrument with an accelerating voltage of 200 kV. TEM samples were prepared by drop-coating of NPs from an ethanol dispersion on a holey carbon-coated copper grid, and the solvent was removed under vacuum. TEM and HRTEM images were processed using ImageJ software (version 1.48 v). Size distribution histograms were determined by measuring *ca.* 300 NPs and plotted as average-shifted histograms. Raman spectroscopy was performed using a Renishaw in*Via* Raman microscope equipped with a 514 nm diode laser and a power of 3.98 mW on the sample. Samples were prepared by drop-casting of an ethanol or water suspension on gold-coated glass. X-ray photoelectron spectra were acquired in energy spectrum mode at 210 W, using a Kratos Axis Ultra X-ray photoelectron spectrometer. X-Ray source was Al (monochromatic) Kα line (λ = 8.34 Å) with the energy at 1486.6 eV. The probing area is about 1 x 2 mm^2. Samples were prepared as films drop-cast from ethanol/water suspensions onto a copper foil substrate. Binding energies were calibrated using the C 1s peak as a reference (284.8 eV). CasaXPS Version 2.3.5 software was used for Shirley background subtraction and curve fitting. Photoluminescence (PL) spectra for the solution phase samples were acquired using a Varian Cary Eclipse fluorescence spectrometer (λ_{ex} = 350 nm). PL spectra were acquired by illuminating a solution/suspension containing desired particles in ethanol (SiQDs) or water (Fe_3O_4 NPs and Si-amide-Fe_3O_4 nano-hybrids).

Synthesis of Water Dispersible APTMS-capped Fe_3O_4 NPs. In a typical synthesis, $FeCl_2 \cdot 4H_2O$ (0.62 g; 3.2 mmol) was dissolved in 3.9 mL of ultrapure water and concentrated aqueous ammonium hydroxide (29.3 wt %; 3.12 ml) was added dropwise with vigorous stirring. The addition of ammonium hydroxide yields a dark blue/green solution. After vigorous stirring under ambient conditions for 10 minutes, APTMS (1.25 ml, 7.2 mmol) was added dropwise (1-3 drops/second). The reaction mixture was transferred to a 10 ml microwave vessel equipped with a microwave-safe stir bar and sealed. The mixture was irradiated for 1 hour at 134 °C in a *Biotage Initiator* microwave reactor (at *ca.* 100 W and the pressure of *ca.* 7 bar). After cooling to room temperature, the reaction vessel was opened, and the resulting black suspension of APTMS-capped Fe_3O_4 NPs was transferred to a PTFE centrifuge tube, and *ca.* 45 ml DI water: acetone, 1 : 3 V/V was added. After centrifuging at 10000 rpm for 15 minutes, the clear supernatant was discarded, and the black precipitate was re-dispersed in water and centrifuged (10000 rpm, 15 minutes). Dispersion/separation cycles were repeated, twice using water and twice using ethanol. Finally, the black precipitate containing purified APTMS-capped Fe_3O_4 NPs were dispersed in *ca.* 10 mL of water and stored in a vial for further analysis using XPS, TEM, EDX, and FTIR.

Preparation of Hydride-Terminated SiQDs. Hydride-terminated SiQDs (H-SiQDs) were prepared using well-established procedures developed in the Veinot laboratory.[101] Approximately 3 g of solid HSQ was placed in a zirconia boat, transferred to a Carbolite CTF tube furnace, and heated in a flowing 5 % H_2 / 95 % Ar atmosphere (*ca.* 15 mL/min) at 18 ºC/min to a peak temperature of 1200 ºC where it was maintained for 1 hr. After cooling to room temperature, the resulting composite, consisting of oxide-embedded SiQDs, was mechanically ground to a fine powder using

an agate mortar and pestle. Subsequently, 0.30 g of the composite powder was transferred to a polyethylene terephthalate beaker, and 3 mL each of water, ethanol, and 49 % HF acid were added sequentially with stirring. (Caution: Appropriate safeguards must be implemented when working with hydrofluoric acid.) After stirring for 1 h in ambient light and atmosphere, hydrophobic H-SiQDs were extracted into three 15 mL aliquots of toluene. The resulting toluene suspensions were centrifuged at 3000 rpm for 5 minutes to obtain a pellet of H-SiQDs that was re-dispersed in dry toluene and used directly in the functionalization procedure described below.

Preparation of Undecanoic-Acid Functionalized SiQDs. Undecanoic acid-terminated SiQDs were prepared using established procedures for radical initiated surface hydrosilylation.[72] A 100 ml Schlenk flask was charged with 10-undecenoic acid (200 mg, 1.1 mmol) equipped with a Teflon-coated magnetic stir bar. The flask was attached to an argon charged double manifold and heated to 70 °C under reduced pressure (*ca.* 2 mbar) for 3 h. After cooling to room temperature, a toluene dispersion of H-SiQDs (*ca.* 25 mg SiQDs in 20 mL dry toluene) and AIBN (0.061 mmol) were added to the flask, and the mixture was subjected to three freeze-pump-thaw cycles. The cloudy reaction mixture was stirred and heated to 65 °C and maintained under an argon atmosphere for at least 15 h. After cooling to room temperature the resulting functionalized particles were isolated by centrifugation (3000 rpm, 10 minutes) and purified by three successive cycles of dispersion/precipitation cycles using methanol/toluene as the solvent/antisolvent mixture. Acid-functionalized SiQDs were dispersible in common polar solvents (e.g., methanol). The resulting products were evaluated using TEM, EDX, XPS, Raman, PL, and FT-IR.

DCC Coupling of Undecanoic Acid-terminated SiQDs with APTMS-capped Fe_3O_4 NPs. In a 20 mL glass vial equipped with magnetic stir bar, 1.0 mL of dicyclohexylcarbodiimide (DCC) in acetone

(0.1 M) was mixed with 10 mL of 10-undecenoic acid-functionalized SiQDs in acetone (2 mg/mL). After capping the vial, the solution was stirred for *ca.* 20 minutes, followed by sonication (*ca.* 30 s) in a bath sonicator. The magnetic stir bar was removed, and 200 µL of APTMS-capped Fe_3O_4 NPs in acetone (20 mg/mL) was added. After capping the vial, it was placed on a vial platform of Orbital Mechanical Shaker at 300 rpm for at least 12 h. The coupled hybrid NPs were isolated upon exposure to a permanent magnet for at least 6 hours. The supernatant was removed, and the magnetic residue was re-dispersed in acetone (*ca.* 10 mL) and sonicated for a minimum of 60 s. The magnetic separation cycles were repeated at least four additional times. After the magnetic residue was re-dispersed in water (*ca.* 10 mL) and sonicated for minimum 60 s. The magnetic separation cycles were repeated two times in water. Purified coupled magnetic Si-amide-Fe_3O_4 NPs were dispersed in water and stored in a vial for further characterization.

RBL-2H3 Cell line. RBL-2H3 cells were grown to confluence at 37 °C with 5% CO_2 in culture media consisting of Minimal Essential Medium (MEM) with Earle's balanced salt solution (Sigma-Aldrich, Canada) supplemented with 1 % two mM L-glutamine, 1% penicillin/streptomycin, and 10 % heat-inactivated FBS as previously described.[102] Cells were passed every third day by harvesting cells in an RBL-2H3 harvest buffer (1.5 mM EDTA, 135 mM NaCl, 20 mM HEPES, five mM KCl, pH 7.4) at 37°C with 5 % CO_2 for 10 minutes, followed by pipetting to detach cells from cell culture plate (BD Biosciences, Mississauga, Canada). Cells were seeded into new flasks at a subcultivation ratio of 1:10.

Annexin V/PI cell apoptosis assay. The Annexin V/PI apoptosis assay was used to measure the effects of Si-amide-Fe_3O_4 NPs on cell viability. Annexin V-FITC binds to damaged membranes undergoing early to late apoptosis. At the same time, the fluorescent molecule, propidium iodide

(PI), penetrates damaged plasma membranes of necrotic and/or late apoptotic cells and intercalates with nucleic acids to enhance its fluorescence. The balance of fluorescence between Annex V-FITC and PI provides a quantitative measure of cells that are i) viable, ii) early apoptotic, iii) late apoptotic, and iv) necrotic. Cells were grown to confluence over 3 days in RBL-2H3 cell culture media and then harvested as above and enumerated with Trypan Blue staining solution (Sigma Aldrich, Canada) on a hemocytometer to ensure cell cultures had >95% viable cells and to determine cell concentration. Following enumeration, cells were resuspended in fresh culture media and seeded in 24-well flat-bottom culture plates (Corning Costar, USA) at 2.5 x 10^5 cells per well. Cells were then incubated for 1 h at 37°C with 5% CO_2 to allow for cell attachment to wells. RBL-2H3 cells were then exposed to Si-amide-Fe_3O_4 NPs at 0, 0.1, 1, 10 and 100 µg/mL for 1 h or 24 h at 37°C with 5% CO_2. Vehicle (equivalent H_2O volume), positive (1 % ethanol), and negative (culture media) control treatments were also included.

Following exposure, cell culture media with NPs was removed from wells, and cells were washed twice with 1x phosphate-buffered saline (PBS; 2.7 mM KCl, 1.5 mM KH_2PO_4, 136.9 mM 148 NaCl, 15.2 mM Na2HPO4; pH 7.0), harvested as above, and transferred to 5 mL polystyrene tubes (Corning Science, Canada) containing 3 mL of PBS supplemented with 0.5 % fetal bovine serum (FBS) (Sigma, Canada) (herein known as PBS-FBS). Cells were centrifuged at 400 x *g* for 7 minutes to pellet cells. The supernatant was decanted, and the cell pellet gently disrupted and resuspended in 1 mL of 1x Annexin V binding buffer (BD Biosciences, Canada). Cells were then centrifuged at 400 x *g* for 7 minutes, followed by decanting supernatant and gently disrupting cell pellet. 5 µL of Annexin V-FITC and 4 µL of 1:10 diluted PI (2 µg/mL) were added to each tube and incubated at room temperature in the dark for 15 minutes. Following incubation, an

additional 500 µL of Annexin V binding buffer was added to each tube and was centrifuged at 400 x *g* for 7 minutes to wash cells. The supernatant was decanted, and cells were resuspended in 500 µL of Annexin V binding buffer and analyzed by flow cytometry for indications of cell death by monitoring for increases in Annexin V-FITC and PI fluorescence, and for changes in cell profile outputs, relative to unexposed controls.

Cellular oxidative stress assay. Cellular oxidative stress was measured in RBL-2H3 cells using the dye 6-carboxy-2,7'-dichlorodihydrofluorescein diacetate, di(acetoxy ester) (DCFH-DA; Sigma Aldrich) following methods previously described by Toduka *et al*.[103] DCFH-DA is a non-fluorescing compound that is taken up by cells and converted to fluorescing dichlorodihydrofluorescein (DCF) in the presence of ROS. RBL-2H3 cells were seeded into 24-well flat-bottom plates as described above at a density of 1.0 x 10^5 cells per well and exposed to PBS-suspended Si-amide-Fe_3O_4 NPs for 1h at 37°C with 5% atmospheric CO_2 at concentrations of 0, 0.1, 1, 10, and 100 µg/mL. Vehicle (equivalent PBS volume) and negative (culture media) control treatments were also included. Cells were exposed to a positive control (200 µM H_2O_2) for 30 min. The exposure media was then removed, and the cells were washed twice in 1x PBS-FBS and resuspended in 500 µL of PBS containing 10 µM DCFH-DA and incubated for 30 min at 37°C in 5% atmospheric CO_2. Following incubation, cells were harvested with harvest buffer as described above, and 10 µL of 1:10 diluted PI (2 µg/mL) was added to each well. ROS generation was detected by DCF fluorescence using flow cytometry (fluorescence of PI measured at 670 nm (FL3) and DCFH-DA at 530/30 nm FL1). Gates were created to eliminate cells expressing PI fluorescence (i.e., dead cells) so that ROS (i.e., DCFH-DA fluorescence) was only measured in the living population of cells.

Inductive heating experiments. RBL-2H3 cells were exposed to Si-amide-Fe_3O_4-exposed NPs as described above for both the AnnexinV-PI and DCFH-DA assays, followed by exposure to an induction furnace heating system to determine if cell death and oxidative stress could be potentiated. Following exposure to NPs in both cell viability assays, the adhered cells were heated in 24-well flat-bottom plates using an EASYHEAT LI inductive heating system with a 7-turn, water-cooled copper coil with an inner diameter of 5.0 cm and an outer diameter of 6.0 cm and a height of 4.5 cm. The well plates were placed under the coil, and heating was performed using a frequency of 156 kHz at currents (powers) of either 100 A (0.2 kW), or 500 A (4 kW) for 1 or 10 min. A picture of the setup can be found in Figure S12. The cells were then immediately harvested as described above and appropriately processed for each assay.

Cell degranulation assay. Cellular immune activation was assessed via the β-hexosaminidase release assay.[104] 5.0 x 10^4 cells were seeded in 24-well flat-bottom plates, as described above. Cells were exposed to PBS-suspended Si-amide-Fe_3O_4 NPs for 1 h at 37^{o}C in 5% atmospheric CO_2 at concentrations of 0, 0.1, 1, 10 and 100 µg/mL. Vehicle (1xPBS) and negative (cell media alone) and positive (Ca^{2+}/PMA (phorbol 12-myristate 13-acetate)) control groups were also included. A second positive control was included an IgE-sensitized and DNP-HSA stimulated group to measure degranulation via Fcε surface membrane receptors (FcεRI), which are targets for environmental antigens. Following exposure, cellular supernatants of NP-exposed cells were incubated with 2 x 10^{-3} M 4-methylumbelliferyl N-acetyl-β-D-glucosaminide as described by Naal *et al*.[104] A Perkin-Elmer microplate reader (360 nm excitation; 450 nm emission) analyzed sample fluorescence. For both positive and negative controls, exposure media was removed and cells were incubated in Tyrode's buffer (25 x 10 −3 M HEPES, 140 x 10^{-3} M NaCl, 1.8 x 10^{-3} M $CaCl_2$, 5.6

x 10^{-3} M D-glucose, 12 x 10^{-3} M $NaHCO_3$, 0.37 x 10^{-3} M NaH_2PO_4, $MgCl_2$, BSA 0.1%, pH 7.4). 100 ng/mL of mouse anti-DNP IgE mAb (Sigma-Aldrich, Canada) was added to sensitize cells in the positive control group, while the other positive (i.e., Ca^{2+}/PMA) and the negative control groups (i.e., cell culture media) received an equivalent volume of Tyrode's buffer. Cells were incubated for 1 h at 37°C with 5% atmospheric CO_2. Solutions were then removed and 0.1 ng/mL DNP-HSA (Biosearch Technologies Inc. USA) was added to IgE-sensitized cells, while 5 ng/mL Ca^{2+}/PMA was added to the other positive control and Tyrode's buffer alone added to the negative control and incubated for 1 h at 37°C with 5% atmospheric CO_2. The levels of β-hex released by cells in each control group were determined by incubating the cellular supernatants as described above. Relative fluorescence units (RFU) collected from the spectrophotometer from all treatment groups, signifying the cellular release of β-hex, were represented as normalized values by setting IgE-sensitized positive control cells to 100%. The relative β-hex release for all samples was then calculated using the following equation [(RFU of experimental treatment - RFU of negative control)/RFU of IgE positive control cells - RFU of negative control) x 100].

Uptake of Si-amide-Fe_3O_4 NPs into RBL-2H3 cells. Confocal microscopy was used to monitor the uptake of Si-amide-Fe_3O_4 NPs into cells. Glass slide coverslips (Fisher Scientific) were sterilized with 70 % ethanol, washed with sterile H_2O, UV irradiated, and placed into the bottom of 6 well flat-bottom plates (Corning Costar, USA). Cells were seeded over top of the cover slips, at a density of 1.0 x 10^5 cells in MEM culture media, and incubated for 2 days at 37 °C. Following 2 days of growth, culture media was removed, coverslips containing adhered cells were washed twice in PBS, and then cells exposed for 1 h to Si-amide-Fe_3O_4 NPs suspended in PBS at concentrations of 0, 100, 200, 500, 1000, and 2000 μg/mL. Negative control cells received an

equal volume of PBS alone. After exposure, cells were washed twice with PBS-FBS, and once with PBS, and coverslips were removed from wells and inverted on parafilm containing 1 µg/µL Cholera Toxin B Subunit-FITC GM1 membrane stain (Sigma) and incubated for 20 minutes over ice in the dark. Coverslips were then washed twice with PBS-FBS and fixed at room temperature in the dark with 4% paraformaldehyde, followed by washing with PBS and mounted on glass slides using mounting medium containing DAPI, as a nuclear stain. Fixed cells were imaged with a Zeiss LSCM, LSM 710 AxioObserver Laser Scanning Confocal Microscope (objective 40x 1.3 oil plan-Apochromat, Carl Zeiss Microscopy, Jena, Germany), data collected with Zen 2011 software and processed with LSM Image Browser (v. 4.2.0.121, Carl Zeiss). Three-dimensional z-stack images were surface rendered and then animated using Imaris software (v. 8.1, Bitplane, Zurich, Switzerland) to visualize intracellular uptake of NPs.

Statistical analysis. Statistical analyses were performed using the GraphPad 6.0 statistical software program. A two-way analysis of variance (ANOVA) was used to investigate the effects of NPs on cell viability. A one-way ANOVA was used to investigate NP effects on oxidative stress and cellular degranulation. A pairwise Tukey multiple comparison test was performed following the ANOVAs for comparisons between treatment groups . A probability of $p < 0.05$ was considered significant. Data values are presented as mean ± standard error on the mean (SEM).

ACKNOWLEDGMENT

The authors recognize generous continued funding from the “Alberta/Technische Universität München Graduate School for Functional Hybrid Materials (ATUMS)” supported by

the Natural Sciences and Engineering Research Council of Canada (NSERC) CREATE program. We also acknowledge continued generous funding from the NSERC Strategic Project Grant Program, Environment Canada and the National Institute of Nanotechnology, the Canada Foundation for Innovation (CFI), and Alberta Innovates to JV and GG. VAO was supported by an Alberta Innovates Health Solutions Graduate Studentship and NSERC Post Graduate Doctoral Scholarship while MJ was supported by the Department of Chemistry, University of Alberta. ANT was supported by the Alberta Innovates Graduate Student Scholarship and the Government of Alberta Queen Elizabeth II Graduate Scholarship. Dr. X. Sun and Geraldine Barron are thanked for their confocal microscopy guidance at the Cross Cancer Institute in Edmonton, Alberta. Dr. Krushelnycky, G. Popowich, C. Lawford, Dr. A. Schultz and W. Moffat are thanked for their technical and/or editorial assistance. Dr. Y. Khaniani and the members of the Veinot and Goss research teams are also thanked for useful discussions.

REFERENCES

(1) Bigall, N. C.; Parak, W. J.; Dorfs, D. Fluorescent, Magnetic and Plasmonic—Hybrid Multifunctional Colloidal Nano Objects. *Nano Today* **2012**, *7*, 282–296.

(2) Suh, W. H.; Suh, Y.-H.; Stucky, G. D. Multifunctional Nanosystems at the Interface of Physical and Life Sciences. *Nano Today* **2009**, *4*, 27–36.

(3) Mahajan, K. D.; Fan, Q.; Ruan, G.; Winter, J. O. Magnetic Quantum Dots in Biotechnology – Synthesis and Applications. **2013**, 1424–1434.

(4) Mahmoudi, M.; Shokrgozar, M. A. Multifunctional Stable Fluorescent Magnetic Nanoparticles. *Chem. Commun.* **2012**, *48*, 3957–3959.

(5) Yang, W. J.; Lee, J. H.; Hong, S. C.; Lee, J.; Lee, J.; Han, D.-W. Difference between Toxicities of Iron Oxide Magnetic Nanoparticles with Various Surface-Functional Groups against Human Normal Fibroblasts and Fibrosarcoma Cells. *Materials (Basel).* **2013**, *6*, 4689–4706.

(6) Corr, S. A.; Rakovich, Y. P.; Gun'ko, Y. K. Multifunctional Magnetic-Fluorescent Nanocomposites for Biomedical Applications. *Nanoscale Res. Lett.* **2008**, *3*, 87–104.

(7) Hu, F. Q.; Wei, L.; Zhou, Z.; Ran, Y. L.; Li, Z.; Gao, M. Y. Preparation of Biocompatible Magnetite Nanocrystals for In Vivo Magnetic Resonance Detection of Cancer. *Adv. Mater.* **2006**, *18*, 2553–2556.

(8) Kolosnjaj-tabi, J.; Wilhelm, C.; Clément, O.; Gazeau, F. Cell Labeling with Magnetic Nanoparticles : Opportunity for Magnetic Cell Imaging and Cell Manipulation. *J. Nanobiotechnology* **2013**, *11*, S7.

(9) Quarta, A.; Corato, R. Di; Manna, L.; Ragusa, A.; Pellegrino, T. Fluorescent-Magnetic Hybrid Nanostructures : Preparation , Properties , and Applications in Biology. **2007**, *6*, 298–308.

(10) Oxide, I. I. I. I.; Erogbogbo, F.; Yong, K.-T.; Hu, R.; Law, W.; Ding, H.; Chang, C.; Prasad, P. N.; Swihart, M. T. Biocompatible Magnetofluorescent Probes: Luminescent Silicon Quantum Dots Coupled with Superparamagnetic Iron(III) Oxide. *ACS Nano* **2010**, *4*, 5131–5138.

(11) Budde, M. D.; Frank, J. A. Magnetic Tagging of Therapeutic Cells for MRI. *J. Nucl. Med.* **2009**, *50*, 171–174.

(12) Murrag, C. B.; Norris, D. B.; Bawendi, M. G. 'Synthesis and Characterization of Nearly Monodisperse CdE (E= S, Se, Te) Semiconductor Nanocrystallite. *J. Am. Chem. Soc* **1993**, *115*, 8706–8715.

(13) Wang, S.; Jarrett, B. R.; Kauzlarich, S. M.; Louie, A. Y. Core/Shell Quantum Dots with High Relaxivity and Photoluminescence for Multimodality Imaging. *J. Am. Chem. Soc.* **2007**, *129*, 3848–3856.

(14) Veiseh, O.; Sun, C.; Gunn, J.; Kohler, N.; Gabikian, P.; Lee, D.; Bhattarai, N.;

Ellenbogen, R.; Sze, R.; Hallahan, A. Optical and MRI Multifunctional Nanoprobe for Targeting Gliomas. *Nano Lett.* **2005**, *5*, 1003–1008.

(15) Ruan, G.; Vieira, G.; Henighan, T.; Chen, A.; Thakur, D.; Sooryakumar, R.; Winter, J. O. Simultaneous Magnetic Manipulation and Fluorescent Tracking of Multiple Individual Hybrid Nanostructures. *Nano Lett.* **2010**, *10*, 2220–2224.

(16) Ang, C. Y.; Giam, L.; Chan, Z. M.; Lin, A. W. H.; Gu, H.; Devlin, E.; Papaefthymiou, G. C.; Selvan, S. T.; Ying, J. Y. Facile Synthesis of Fe2O3 Nanocrystals without Fe(CO)5 Precursor and One-Pot Synthesis of Highly Fluorescent Fe2O3–CdSe Nanocomposites. *Adv. Mater.* **2009**, *21*, 869–873.

(17) Chen, O.; Riedemann, L.; Etoc, F.; Herrmann, H.; Coppey, M.; Barch, M.; Farrar, C. T.; Zhao, J.; Bruns, O. T.; Wei, H.; et al. Magneto-Fluorescent Core-Shell Supernanoparticles. *Nat. Commun.* **2014**, *5*, 5093.

(18) Grim, J. Q.; Manna, L.; Moreels, I. A Sustainable Future for Photonic Colloidal Nanocrystals. *Chem. Soc. Rev.* **2015**, *44*, 5897–5914.

(19) Marcelo, G. A.; Lodeiro, C.; Capelo, J. L.; Lorenzo, J.; Oliveira, E. Magnetic, Fluorescent and Hybrid Nanoparticles: From Synthesis to Application in Biosystems. *Mater. Sci. Eng. C* **2020**, *106*, 110104.

(20) Bimbo, L. M.; Sarparanta, M.; Santos, H. A.; Airaksinen, A. J.; Mäkilä, E.; Laaksonen, T.; Peltonen, L.; Lehto, V.-P.; Hirvonen, J.; Salonen, J. Biocompatibility of Thermally Hydrocarbonized Porous Silicon Nanoparticles and Their Biodistribution in Rats. *ACS Nano* **2010**, *4*, 3023–3032.

(21) Park, J.-H.; Gu, L.; Von Maltzahn, G.; Ruoslahti, E.; Bhatia, S. N.; Sailor, M. J. Biodegradable Luminescent Porous Silicon Nanoparticles for in Vivo Applications. *Nat. Mater.* **2009**, *8*, 331–336.

(22) Romano, F.; Angeloni, S.; Morselli, G.; Mazzaro, R.; Morandi, V.; Shell, J. R.; Cao, X.; Pogue, B. W.; Ceroni, P. Water-Soluble Silicon Nanocrystals as NIR Luminescent Probes for Time-Gated Biomedical Imaging. *Nanoscale* **2020**, *12*, 7921–7926.

(23) Islam, M. A.; Sinelnikov, R.; Howlader, M. A.; Faramus, A.; Veinot, J. G. C. Mixed Surface Chemistry: An Approach to Highly Luminescent Biocompatible Amphiphilic Silicon Nanocrystals. *Chem. Mater.* **2018**, *30*, 8925–8931.

(24) Fujioka, K.; Hiruoka, M.; Sato, K.; Manabe, N.; Miyasaka, R.; Hanada, S.; Hoshino, A.; Tilley, R. D.; Manome, Y.; Hirakuri, K. Luminescent Passive-Oxidized Silicon Quantum Dots as Biological Staining Labels and Their Cytotoxicity Effects at High Concentration. *Nanotechnology* **2008**, *19*, 415102.

(25) Pramanik, S.; Hill, S. K. E.; Zhi, B.; Hudson-Smith, N. V.; Wu, J. J.; White, J. N.; McIntire, E. A.; Kondeti, V. S. S. K.; Lee, A. L.; Bruggeman, P. J.; et al. Comparative Toxicity Assessment of Novel Si Quantum Dots and Their Traditional Cd-Based Counterparts Using Bacteria Models Shewanella Oneidensis and Bacillus Subtilis. *Environ. Sci. Nano* **2018**, *5*, 1890–1901.

(26) Ge, S.; Shi, X.; Sun, K.; Li, C.; Uher, C.; Baker, J. R.; Banaszak Holl, M. M.; Orr, B. G.;

Baker Jr, J. R.; Banaszak Holl, M. M.; et al. Facile Hydrothermal Synthesis of Iron Oxide Nanoparticles with Tunable Magnetic Properties. *J. Phys. Chem. C* **2009**, *113*, 13593–13599.

(27) Gonzales, M.; Mitsumori, L. M.; Kushleika, J. V; Rosenfeld, M. E.; Krishnan, K. M. Cytotoxicity of Iron Oxide Nanoparticles Made from the Thermal Decomposition of Organometallics and Aqueous Phase Transfer with Pluronic F127. *Contrast Media Mol. Imaging* **2010**, *5*, 286–293.

(28) Tromsdorf, U. I.; Bruns, O. T.; Salmen, S. C.; Beisiegel, U.; Weller, H. A Highly Effective, Nontoxic T 1 MR Contrast Agent Based on Ultrasmall PEGylated Iron Oxide Nanoparticles. *Nano Lett.* **2009**, *9*, 4434–4440.

(29) Wang, Y.-X. J.; Hussain, S. M.; Krestin, G. P. Superparamagnetic Iron Oxide Contrast Agents: Physicochemical Characteristics and Applications in MR Imaging. *Eur. Radiol.* **2001**, *11*, 2319–2331.

(30) Wang, Y.-X. J. Superparamagnetic Iron Oxide Based MRI Contrast Agents: Current Status of Clinical Application. *Quant. Imaging Med. Surg.* **2011**, *1*, 35.

(31) Pouliquen, D.; Le Jeune, J. J.; Perdrisot, R.; Ermias, A.; Jallet, P. Iron Oxide Nanoparticles for Use as an MRI Contrast Agent: Pharmacokinetics and Metabolism. *Magn. Reson. Imaging* **1991**, *9*, 275–283.

(32) Wei, H.; Bruns, O. T.; Kaul, M. G.; Hansen, E. C.; Barch, M.; Wiśniowska, A.; Chen, O.; Chen, Y.; Li, N.; Okada, S. Exceedingly Small Iron Oxide Nanoparticles as Positive MRI Contrast Agents. *Proc. Natl. Acad. Sci.* **2017**, *114*, 2325–2330.

(33) Bernd, H.; De Kerviler, E.; Gaillard, S.; Bonnemain, B. Safety and Tolerability of Ultrasmall Superparamagnetic Iron Oxide Contrast Agent: Comprehensive Analysis of a Clinical Development Program. *Invest. Radiol.* **2009**, *44*, 336–342.

(34) Gilchrist, R. K.; Medal, R.; Shorey, W. D.; Hanselman, R. C.; Parrott, J. C.; Taylor, C. B. Selective Inductive Heating of Lymph Nodes. *Ann. Surg.* **1957**, *146*, 596.

(35) Cardoso, V. F.; Francesko, A.; Ribeiro, C.; Bañobre-López, M.; Martins, P.; Lanceros-Mendez, S. Advances in Magnetic Nanoparticles for Biomedical Applications. *Adv. Healthc. Mater.* **2018**, *7*, 1700845.

(36) Jang, J.; Lee, J.; Seon, J.; Ju, E.; Kim, M.; Kim, Y. Il; Kim, M. G.; Takemura, Y.; Arbab, A. S.; Kang, K. W. Giant Magnetic Heat Induction of Magnesium-Doped Γ-Fe2O3 Superparamagnetic Nanoparticles for Completely Killing Tumors. *Adv. Mater.* **2018**, *30*, 1704362.

(37) Avugadda, S. K.; Materia, M. E.; Nigmatullin, R.; Cabrera, D.; Marotta, R.; Cabada, T. F.; Marcello, E.; Nitti, S.; Artés-Ibañez, E. J.; Basnett, P. Esterase-Cleavable 2D Assemblies of Magnetic Iron Oxide Nanocubes: Exploiting Enzymatic Polymer Disassembling To Improve Magnetic Hyperthermia Heat Losses. *Chem. Mater.* **2019**, *31*, 5450–5463.

(38) Nemati, Z.; Alonso, J.; Rodrigo, I.; Das, R.; Garaio, E.; García, J. Á.; Orue, I.; Phan, M.-H.; Srikanth, H. Improving the Heating Efficiency of Iron Oxide Nanoparticles by Tuning Their Shape and Size. *J. Phys. Chem. C* **2018**, *122*, 2367–2381.

(39) Sánchez-Cabezas, S.; Montes-Robles, R.; Gallo, J.; Sancenón, F.; Martínez-Máñez, R. Combining Magnetic Hyperthermia and Dual T 1/T 2 MR Imaging Using Highly Versatile Iron Oxide Nanoparticles. *Dalt. Trans.* **2019**, *48*, 3883–3892.

(40) Espinosa, A.; Kolosnjaj-Tabi, J.; Abou-Hassan, A.; Plan Sangnier, A.; Curcio, A.; Silva, A. K. A.; Di Corato, R.; Neveu, S.; Pellegrino, T.; Liz-Marzán, L. M. Magnetic (Hyper) Thermia or Photothermia? Progressive Comparison of Iron Oxide and Gold Nanoparticles Heating in Water, in Cells, and in Vivo. *Adv. Funct. Mater.* **2018**, *28*, 1803660.

(41) Xu, Y.; Karmakar, A.; Wang, D.; Mahmood, M. W.; Watanabe, F.; Zhang, Y.; Fejleh, A.; Fejleh, P.; Li, Z.; Kannarpady, G. Multifunctional Fe3O4 Cored Magnetic-Quantum Dot Fluorescent Nanocomposites for RF Nanohyperthermia of Cancer Cells. *J. Phys. Chem. C* **2010**, *114*, 5020–5026.

(42) Palmer, R. K.; Hutchinson, L. M.; Burpee, B. T.; Tupper, E. J.; Pelletier, J. H.; Kormendy, Z.; Hopke, A. R.; Malay, E. T.; Evans, B. L.; Velez, A. Antibacterial Agent Triclosan Suppresses RBL-2H3 Mast Cell Function. *Toxicol. Appl. Pharmacol.* **2012**, *258*, 99–108.

(43) Ortega, V. A.; Ede, J. D.; Boyle, D.; Stafford, J. L.; Goss, G. G. Polymer-Coated Metal-Oxide Nanoparticles Inhibit IgE Receptor Binding, Cellular Signaling, and Degranulation in a Mast Cell-like Cell Line. *Adv. Sci.* **2015**, *2*.

(44) Chen, S.; Gong, J.; Liu, F.; Mohammed, U. Naturally Occurring Polyphenolic Antioxidants Modulate IgE-mediated Mast Cell Activation. *Immunology* **2000**, *100*, 471–480.

(45) Feltis, B. N.; Elbaz, A.; Wright, P. F. A.; Mackay, G. A.; Turney, T. W.; Lopata, A. L. Characterizing the Inhibitory Action of Zinc Oxide Nanoparticles on Allergic-Type Mast Cell Activation. *Mol. Immunol.* **2015**, *66*, 139–146.

(46) Ede, J. D.; Ortega, V. A.; Boyle, D.; Beingessner, R. L.; Hemraz, U. D.; Fenniri, H.; Stafford, J. L.; Goss, G. G. Rosette Nanotubes Alter IgE-Mediated Degranulation in the Rat Basophilic Leukemia (RBL)-2H3 Cell Line. *Toxicol. Sci.* **2015**, kfv166.

(47) Gilfillan, A. M.; Tkaczyk, C. Integrated Signalling Pathways for Mast-Cell Activation. *Nat. Rev. Immunol.* **2006**, *6*, 218–230.

(48) Massol, P.; Montcourrier, P.; Guillemot, J.; Chavrier, P. Fc Receptor-mediated Phagocytosis Requires CDC42 and Rac1. *EMBO J.* **1998**, *17*, 6219–6229.

(49) Sun, S.; Zeng, H.; Robinson, D. B.; Raoux, S.; Rice, P. M.; Wang, S. X.; Li, G. Monodisperse MFe2O4 (M= Fe, Co, Mn) Nanoparticles. *J. Am. Chem. Soc.* **2004**, *126*, 273–279.

(50) Bao, N.; Shen, L.; Wang, Y.; Padhan, P.; Gupta, A. Ref 27-A Facile Thermolysis Route to Monodisperse Ferrite Nanocrystals. *J. Am. Chem. Soc.* **2007**, *129*, 12374–12375.

(51) Sun, S.; Zeng, H. Size-Controlled Synthesis of Magnetite Nanoparticles. *J. Am. Chem. Soc.* **2002**, *124*, 8204–8205.

(52) Pavía-Sanders, A.; Zhang, S.; Flores, J. A ; Sanders, J. E.; Raymond, J. E.; Wooley, K. L. Robust Magnetic (SI)/Polymer Hybrid Nanoparticles Designed for Crude Oil

Entrapment and Recovery in Aqueous Environments. *ACS Nano* **2013**, No. Xx, 1–6.

(53) Shen, M.; Cai, H.; Wang, X.; Cao, X.; Li, K.; Wang, S. H.; Guo, R.; Zheng, L.; Zhang, G.; Shi, X. Facile One-Pot Preparation, Surface Functionalization, and Toxicity Assay of APTS-Coated Iron Oxide Nanoparticles. *Nanotechnology* **2012**, *23*, 105601.

(54) Hu, F.; Li, Z.; Tu, C.; Gao, M. Preparation of Magnetite Nanocrystals with Surface Reactive Moieties by One-Pot Reaction. *J. Colloid Interface Sci.* **2007**, *311*, 469–474.

(55) Xie, J.; Chen, K.; Lee, H.-Y.; Xu, C.; Hsu, A. R.; Peng, S.; Chen, X.; Sun, S. Ultrasmall c(RGDyK)-Coated Fe3O4 Nanoparticles and Their Specific Targeting to Integrin Avβ3-Rich Tumor Cells. *J. Am. Chem. Soc.* **2008**, *130*, 7542–7543.

(56) Mohapatra, S.; Pramanik, N.; Mukherjee, S.; Ghosh, S. K.; Pramanik, P. A Simple Synthesis of Amine-Derivatised Superparamagnetic Iron Oxide Nanoparticles for Bioapplications. *J. Mater. Sci.* **2007**, *42*, 7566–7574.

(57) Eltouny, N.; Ariya, P. A. Competing Reactions of Selected Atmospheric Gases on Fe 3 O 4 Nanoparticles Surfaces. *Phys. Chem. Chem. Phys.* **2014**, *16*, 23056–23066.

(58) Wilson, D.; Langell, M. A. XPS Analysis of Oleylamine/Oleic Acid Capped Fe3O4 Nanoparticles as a Function of Temperature. *Appl. Surf. Sci.* **2014**, *303*, 6–13.

(59) Fan, T.; Pan, D.; Zhang, H. Study on Formation Mechanism by Monitoring the Morphology and Structure Evolution of Nearly Monodispersed Fe3O4 Submicroparticles with Controlled Particle Sizes. *Ind. Eng. Chem. Res.* **2011**, *50*, 9009–9018.

(60) Eltouny, N. A.; Ariya, P. A. Fe 3O 4 Nanoparticles and Carboxymethyl Cellulose: A Green Option for the Removal of Atmospheric Benzene, Toluene, Ethylbenzene, and o -Xylene (BTEX). *Ind. Eng. Chem. Res.* **2012**, *51*, 12787–12795.

(61) Poulin, S.; França, R.; Moreau-Bélanger, L.; Sacher, E. Confirmation of X-Ray Photoelectron Spectroscopy Peak Attributions of Nanoparticulate Iron Oxides, Using Symmetric Peak Component Line Shapes. *J. Phys. Chem. C* **2010**, *114*, 10711–10718.

(62) Descostes, M.; Mercier, F.; Thromat, N.; Beaucaire, C.; Gautier-Soyer, M. Use of XPS in the Determination of Chemical Environment and Oxidation State of Iron and Sulfur Samples: Constitution of a Data Basis in Binding Energies for Fe and S Reference Compounds and Applications to the Evidence of Surface Species of an Oxidized Py. *Appl. Surf. Sci.* **2000**, *165*, 288–302.

(63) Laurent, S.; Forge, D.; Port, M.; Roch, A.; Robic, C.; Vander Elst, L.; Muller, R. N. Magnetic Iron Oxide Nanoparticles: Synthesis, Stabilization, Vectorization, Physicochemical Characterizations, and Biological Applications. *Chem. Rev.* **2008**, *108*, 2064–2110.

(64) Lu, A.; Salabas, E. emsp14L; Schüth, F. Magnetic Nanoparticles: Synthesis, Protection, Functionalization, and Application. *Angew. Chemie Int. Ed.* **2007**, *46*, 1222–1244.

(65) Huber, D. L. Synthesis, Properties, and Applications of Iron Nanoparticles. *Small* **2005**, *1*, 482–501.

(66) Xu, H.; Zhu, X.; Sun, K.; Liu, Y.; Xie, X. Elaborately Designed Hierarchical Heterostructures Consisting of Carbon-Coated TiO2 (B) Nanosheets Decorated with Fe3O4 Nanoparticles for Remarkable Synergy in High-Rate Lithium Storage. *Adv. Mater. Interfaces* **2015**, *2*.

(67) Goldstein, J.; Newbury, D. E.; Echlin, P.; Joy, D. C.; Romig Jr, A. D.; Lyman, C. E.; Fiori, C.; Lifshin, E. *Scanning Electron Microscopy and X-Ray Microanalysis: A Text for Biologists, Materials Scientists, and Geologists*; Springer Science & Business Media, 2012.

(68) Purkait, T. K.; Iqbal, M.; Wahl, M. H.; Gottschling, K.; Gonzalez, C. M.; Islam, M. A.; Veinot, J. G. C. Borane-Catalyzed Room-Temperature Hydrosilylation of Alkenes/Alkynes on Silicon Nanocrystal Surfaces. *J. Am. Chem. Soc.* **2014**, *136*, 17914–17917.

(69) Chen, Z.; Hu, J.; Lu, Z.; He, X. Low-Temperature Preparation of Lanthanum-Doped BiFeO 3 Crystallites by a Sol–Gel-Hydrothermal Method. *Ceram. Int.* **2011**, *37*, 2359–2364.

(70) Bordbar, A. K.; Rastegari, A. A.; Amiri, R.; Ranjbakhsh, E.; Abbasi, M.; Khosropour, A. R. Characterization of Modified Magnetite Nanoparticles for Albumin Immobilization. *Biotechnol. Res. Int.* **2014**, *2014*.

(71) Hessel, C. M.; Henderson, E. J.; Veinot, J. G. C.; Uni, V.; February, R. V; Re, V.; Recei, M.; August, V. A Molecular Precursor for Nanocrystalline Si - SiO2 Composites and Freestanding Hydride-Surface-Terminated Silicon Nanoparticles. *Chem. Mater.* **2006**, *18*, 6139–6146.

(72) Yang, Z.; Gonzalez, C. M.; Purkait, T. K.; Iqbal, M.; Meldrum, A.; Veinot, J. G. C. Radical Initiated Hydrosilylation on Silicon Nanocrystal Surfaces: An Evaluation of Functional Group Tolerance and Mechanistic Study. *Langmuir* **2015**, *31*, 10540–10548.

(73) Dasog, M.; Yang, Z.; Regli, S.; Atkins, T. M.; Faramus, A.; Singh, M. P.; Muthuswamy, E.; Kauzlarich, S. M.; Tilley, R. D.; Veinot, J. G. C. Chemical Insight into the Origin of Red and Blue Photoluminescence Arising from Freestanding Silicon Nanocrystals. *ACS Nano* **2013**, *7*, 2676–2685.

(74) Robidillo, C. J. T.; Islam, M. A.; Aghajamali, M.; Faramus, A.; Sinelnikov, R.; Zhang, X.; Boekhoven, J.; Veinot, J. G. C. Functional Bioinorganic Hybrids from Enzymes and Luminescent Silicon-Based Nanoparticles. *Langmuir* **2018**, *34*, 6556–6569.

(75) Sheehan, J. C.; Hess, G. P.; Lerner, A. B.; Lee, T. E. H. H. A New Method of Forming Peptide Bonds. *J. Am. Chem. Soc.* **1955**, *77*, 1067–1068.

(76) Neises, B.; Steglich, W. Simple Method for the Esterification of Carboxylic Acids. *Angew. Chemie Int. Ed. English* **1978**, *17*, 522–524.

(77) Alsaleh, N. B.; Persaud, I.; Brown, J. M. Silver Nanoparticle-Directed Mast Cell Degranulation Is Mediated through Calcium and PI3K Signaling Independent of the High Affinity IgE Receptor. *PLoS One* **2016**, *11*, e0167366.

(78) Wilkinson, K.; Ekstrand-Hammarström, B.; Ahlinder, L.; Guldevall, K.; Pazik, R.;

Kępiński, L.; Kvashnina, K. O.; Butorin, S. M.; Brismar, H.; Önfelt, B. Visualization of Custom-Tailored Iron Oxide Nanoparticles Chemistry, Uptake, and Toxicity. *Nanoscale* **2012**, *4*, 7383–7393.

(79) AshaRani, P. V.; Low Kah Mun, G.; Hande, M. P.; Valiyaveettil, S. Cytotoxicity and Genotoxicity of Silver Nanoparticles in Human Cells. *ACS Nano* **2008**, *3*, 279–290.

(80) Sharma, J.; Rocha, R. C.; Phipps, M. L.; Yeh, H.-C.; Balatsky, K. A.; Vu, D. M.; Shreve, A. P.; Werner, J. H.; Martinez, J. S. A DNA-Templated Fluorescent Silver Nanocluster with Enhanced Stability. *Nanoscale* **2012**, *4*, 4107–4110.

(81) Elmore, S. Apoptosis: A Review of Programmed Cell Death. *Toxicol. Pathol.* **2007**, *35*, 495–516.

(82) Kroemer, G.; Galluzzi, L.; Vandenabeele, P.; Abrams, J.; Alnemri, E. S.; Baehrecke, E. H.; Blagosklonny, M. V; El-Deiry, W. S.; Golstein, P.; Green, D. R. Classification of Cell Death: Recommendations of the Nomenclature Committee on Cell Death 2009. *Cell Death Differ.* **2009**, *16*, 3–11.

(83) Galluzzi, L.; Vitale, I.; Abrams, J. M.; Alnemri, E. S.; Baehrecke, E. H.; Blagosklonny, M. V; Dawson, T. M.; Dawson, V. L.; El-Deiry, W. S.; Fulda, S. Molecular Definitions of Cell Death Subroutines: Recommendations of the Nomenclature Committee on Cell Death 2012. *Cell Death Differ.* **2012**, *19*, 107–120.

(84) Kou, L.; Sun, J.; Zhai, Y.; He, Z. The Endocytosis and Intracellular Fate of Nanomedicines: Implication for Rational Design. *Asian J. Pharm. Sci.* **2013**, *8*, 1–10.

(85) Ede, J. D.; Ortega, V. A.; Boyle, D.; Beingessner, R. L.; Hemraz, U. D.; Fenniri, H.; Stafford, J. L.; Goss, G. G. The Effects of Rosette Nanotubes with Different Functionalizations on Channel Catfish (Ictalurus Punctatus) Lymphocyte Viability and Receptor Function. *Environ. Sci. Nano* **2016**, *3*, 578–592.

(86) Zhao, F.; Zhao, Y.; Liu, Y.; Chang, X.; Chen, C.; Zhao, Y. Cellular Uptake, Intracellular Trafficking, and Cytotoxicity of Nanomaterials. *small* **2011**, *7*, 1322–1337.

(87) Lewinski, N.; Colvin, V.; Drezek, R. Cytotoxicity of Nanoparticles. *small* **2008**, *4*, 26–49.

(88) Datta, K. K. R.; Kozak, O.; Ranc, V.; Havrdova, M.; Bourlinos, A. B.; Šafářová, K.; Hola, K.; Tomankova, K.; Zoppellaro, G.; Otyepka, M. Quaternized Carbon Dot-Modified Graphene Oxide for Selective Cell Labelling–Controlled Nucleus and Cytoplasm Imaging. *Chem. Commun.* **2014**, *50*, 10782–10785.

(89) Kumawat, M. K.; Thakur, M.; Gurung, R. B.; Srivastava, R. Graphene Quantum Dots for Cell Proliferation, Nucleus Imaging, and Photoluminescent Sensing Applications. *Sci. Rep.* **2017**, *7*, 1–16.

(90) Lovrić, J.; Bazzi, H. S.; Cuie, Y.; Fortin, G. R. A.; Winnik, F. M.; Maysinger, D. Differences in Subcellular Distribution and Toxicity of Green and Red Emitting CdTe Quantum Dots. *J. Mol. Med.* **2005**, *83*, 377–385.

(91) Maity, A. R.; Stepensky, D. Efficient Subcellular Targeting to the Cell Nucleus of Quantum Dots Densely Decorated with a Nuclear Localization Sequence Peptide. *ACS*

Appl. Mater. Interfaces **2016**, *8*, 2001–2009.

(92) Reifarth, M.; Schubert, U. S.; Hoeppener, S. Considerations for the Uptake Characteristic of Inorganic Nanoparticles into Mammalian Cells—Insights Gained by TEM Investigations. *Adv. Biosyst.* **2018**, *2*, 1700254.

(93) Feng, Q.; Liu, Y.; Huang, J.; Chen, K.; Huang, J.; Xiao, K. Uptake, Distribution, Clearance, and Toxicity of Iron Oxide Nanoparticles with Different Sizes and Coatings. *Sci. Rep.* **2018**, *8*, 1–13.

(94) Hauser, A. K.; Mitov, M. I.; Daley, E. F.; McGarry, R. C.; Anderson, K. W.; Hilt, J. Z. Targeted Iron Oxide Nanoparticles for the Enhancement of Radiation Therapy. *Biomaterials* **2016**, *105*, 127–135.

(95) Tammam, S. N.; Azzazy, H. M. E.; Lamprecht, A. How Successful Is Nuclear Targeting by Nanocarriers? *J. Control. Release* **2016**, *229*, 140–153.

(96) Young, J. H.; Wang, M.-T.; Brezovich, I. A. Frequency/Depth-Penetration Considerations in Hyperthermia by Magnetically Induced Currents. *Electron. Lett.* **1980**, *16*, 358–359.

(97) Curcio, A.; Silva, A. K. A.; Cabana, S.; Espinosa, A.; Baptiste, B.; Menguy, N.; Wilhelm, C.; Abou-Hassan, A. Iron Oxide Nanoflowers@ CuS Hybrids for Cancer Tri-Therapy: Interplay of Photothermal Therapy, Magnetic Hyperthermia and Photodynamic Therapy. *Theranostics* **2019**, *9*, 1288.

(98) Zhang, T.; Li, Y.; Hong, W.; Chen, Z.; Peng, P.; Yuan, S.; Qu, J.; Xiao, M.; Xu, L. Glucose Oxidase and Polydopamine Functionalized Iron Oxide Nanoparticles: Combination of the Photothermal Effect and Reactive Oxygen Species Generation for Dual-Modality Selective Cancer Therapy. *J. Mater. Chem. B* **2019**, *7*, 2190–2200.

(99) Felix, L. C.; Ortega, V. A.; Ede, J. D.; Goss, G. G. Physicochemical Characteristics of Polymer-Coated Metal-Oxide Nanoparticles and Their Toxicological Effects on Zebrafish (Danio Rerio) Development. *Environ. Sci. Technol.* **2013**, *47*, 6589–6596.

(100) Ortega, V. A.; Cameron, M. S.; Stafford, J.; Goss, G. G.; Donald, J. A.; Schultz, A. Polyacrylic Acid Coated Nanoparticles Elicit Endothelial Cell Apoptosis and Diminish Vascular Relaxation in Ex Vivo Perfused Iliac Arteries of the Cane Toad (Rhinella Marina). *Environ. Sci. Nano* **2020**.

(101) Hessel, C. M.; Henderson, E. J.; Veinot, J. G. C. An Investigation of the Formation and Growth of Oxide-Embedded Silicon Nanocrystals in Hydrogen Silsesquioxane-Derived Nanocomposites. *J. Phys. Chem. C* **2007**, *111*, 6956–6961.

(102) Cortes, H. D.; Montgomery, B. C.; Verheijen, K.; García-García, E.; Stafford, J. L. Examination of the Stimulatory Signaling Potential of a Channel Catfish Leukocyte Immune-Type Receptor and Associated Adaptor. *Dev. Comp. Immunol.* **2011**.

(103) Toduka, Y.; Toyooka, T.; Ibuki, Y. Flow Cytometric Evaluation of Nanoparticles Using Side-Scattered Light and Reactive Oxygen Species-Mediated Fluorescence–Correlation with Genotoxicity. *Environ. Sci. Technol.* **2012**, *46*, 7629–7636.

(104) Naal, R. M. Z. G.; Tabb, J.; Holowka, D.; Baird, B. In Situ Measurement of Degranulation

as a Biosensor Based on RBL-2H3 Mast Cells. *Biosens. Bioelectron.* **2004**, *20*, 791–796.